The asymptotic tidal remnants of cold dark matter subhaloes

Raphaël Errani, Julio F. Navarro

Monthly Notices of the ROYAL ASTRONOMICAL SOCIETY

MNRAS **505,** 18–32 (2021) doi:10.1093/mnras/stab1215
Advance Access publication 2021 May 07

The asymptotic tidal remnants of cold dark matter subhaloes

Raphaël Errani[1,2]★ and Julio F. Navarro[1]

[1]*Department of Physics and Astronomy, University of Victoria, Victoria, BC V8P 5C2, Canada*
[2]*Observatoire Astronomique, Université de Strasbourg, CNRS, 11 rue de l'Université, F-67000 Strasbourg, France*

Accepted 2021 April 22. Received 2021 April 22; in original form 2020 November 16

ABSTRACT

We use *N*-body simulations to study the evolution of cuspy cold dark matter (CDM) haloes in the gravitational potential of a massive host. Tidal mass-losses reshape CDM haloes, leaving behind bound remnants whose characteristic densities are set by the mean density of the host at the pericentre of their respective orbit. The evolution to the final bound remnant state is essentially complete after ∼5 orbits for nearly circular orbits, while reaching the same remnant requires, for the same pericentre, ∼25 and ∼40 orbits for eccentric orbits with 1:5 and 1:20 pericentre-to-apocentre ratios, respectively. The density profile of tidal remnants is fully specified by the fraction of mass lost, and approaches an exponentially truncated Navarro–Frenk–White profile in the case of heavy mass-loss. Resolving tidal remnants requires excellent numerical resolution; poorly resolved subhaloes have systematically lower characteristic densities and are more easily disrupted. Even simulations with excellent spatial and time resolution fail when the final remnant is resolved with fewer than 3000 particles. We derive a simple empirical model that describes the evolution of the mass and the density profile of the tidal remnant applicable to a wide range of orbital eccentricities and pericentric distances. Applied to the Milky Way, our results suggest that 10^8–$10^{10}\,M_\odot$ haloes accreted ∼ 10 Gyr ago on 1:10 orbits with pericentric distance ∼ 10 kpc should have been stripped to 0.1–1 per cent of their original mass. This implies that estimates of the survival and structure of such haloes (the possible hosts of ultra-faint Milky Way satellites) based on direct cosmological simulations may be subject to substantial revision.

Key words: dark matter – galaxies: evolution – galaxies: dwarf – methods: numerical.

1 INTRODUCTION

It is well established that structure in a universe dominated by cold dark matter (CDM) evolves hierarchically and leads to the formation of non-linear systems spanning an enormous range in mass (White & Rees 1978; Frenk & White 2012). The basic units of this clustering hierarchy are CDM haloes, virialized entities that form largely through the accretion, disruption, and merging of thousands of smaller subunits (e.g. Wang et al. 2020, and references therein). This complex merging process leaves behind an embedded population of 'subhaloes'; i.e. the remnants of accreted subunits, many of which, despite shedding a large fraction of their initial mass, survive as recognizable self-bound entities for many orbital times (Tormen, Bouchet & White 1997; Ghigna et al. 1998; Klypin et al. 1999; Moore et al. 1999).

It is now accepted that this halo *substructure* is a basic falsifiable prediction of the CDM paradigm, and underpins a number of observational efforts designed to probe the nature of dark matter on sub-galactic scales. Indeed, the role of substructure is critical to the interpretation of observational studies including, for example, (i) possible 'gaps' in the tidal streams of disrupting globular clusters (e.g. Ibata et al. 2002; Johnston, Spergel & Haydn 2002; Erkal & Belokurov 2015); (ii) perturbations in strongly lensed images of distant objects (e.g. Vegetti & Koopmans 2009; Despali & Vegetti 2017); (iii) the number and long-term survival of faint satellite galaxies in the Galactic potential (e.g. Peñarrubia, Navarro & McConnachie 2008; Sanders, Evans & Dehnen 2018; Li et al. 2018); and (iv) the 'boost factor' of a potential dark matter annihilation signal (e.g. Tasitsiomi & Olinto 2002; Diemand, Kuhlen & Madau 2007a; Lavalle et al. 2007; Springel et al. 2008b; Stref, Lacroix & Lavalle 2019).

Because of its complex origin, substructure in CDM haloes is best studied via direct cosmological simulations, which have over the years converged on a basic outline of its basic properties. In the absence of baryons, for example, substructure is expected to be approximately self-similar, in the sense that the subhalo mass function, scaled to the host mass, rises steeply towards small masses and is similar for all virialized haloes (Kravtsov, Gnedin & Klypin 2004; Boylan-Kolchin et al. 2010; Wang et al. 2012; Jiang & van den Bosch 2016b). It is also widely accepted that substructure makes up only a small fraction (∼5–10 per cent) of the total mass of a halo, and that the subhalo spatial distribution and orbital properties are roughly independent of subhalo mass, especially at the low-mass end (Springel et al. 2008a; Ludlow et al. 2009).

Despite these advances, many substantive questions remain, especially those pertaining to the long-term survival of CDM subhaloes and to the role of the central galaxy in aiding their tidal disruption (e.g. Johnston et al. 2002; Hayashi et al. 2003; D'Onghia et al. 2010; Errani et al. 2017; Garrison-Kimmel et al. 2017; van den Bosch & Ogiya 2018). Also unclear is the final structure of heavily stripped CDM subhaloes, and the influence of numerical limitations on these

★ E-mail: errani@unistra.fr

results. These are important questions to resolve, as they may affect sensitively the theoretical interpretation of ongoing dark matter direct and indirect searches (see e.g. Green 2005, and references therein).

The issue of the long-term survival of CDM subhaloes has been addressed in the past. While early work advocated for full subhalo disruption under certain conditions (see e.g. Hayashi et al. 2003), more recent work has argued that, if the density profile of CDM haloes is indeed cuspy (i.e. $\mathrm{d}\ln\rho/\mathrm{d}\ln r = -1$ at the centre) as in the Navarro–Frenk–White profile (Navarro, Frenk & White 1996, 1997, hereafter NFW), then subhaloes would rarely be fully disrupted and some form of bound remnant would almost always survive (e.g. Peñarrubia et al. 2010; van den Bosch et al. 2018). This is motivated by the fact that cuspy haloes contain a substantial population of particles with extremely short orbital time-scales (Errani & Peñarrubia 2020), which would always be 'adiabatically protected' (Weinberg 1994) from the effects of tides.

Although there is growing consensus about this result, we note that it is unlikely to lead to a radical revision of the global properties of CDM substructure described above, which is dominated by subhaloes affected only moderately by tidal effects. However, it may have important consequences for some detailed applications, especially those concerning substructure in the inner regions of a halo, where crossing times are short, where tides are most important, and where many observational studies focus on.

A related issue is the structure of tidally disrupted CDM subhaloes, and, in particular, that of the final bound remnant, if indeed one survives. Prior work suggests that, as tides gradually truncate a subhalo, its characteristic parameters (i.e. radius, density, and circular velocity) evolve along well-defined 'tidal tracks' (Peñarrubia et al. 2008). There is, however, less consensus on how to describe the density profile of tidally stripped subhaloes; on how the final remnant properties depend on the strength of the tidal field; or on how long (i.e. number of orbits) it would take a subhalo to approach its asymptotic final state.

These are the issues we address here using idealized *N*-body simulations to follow the tidal loss/disruption of NFW haloes in the potential of a massive host. The emphasis of our work is on the structure of the asymptotic tidal remnant of such haloes, and on the time-scale on which the process evolves. This paper is structured as follow. Section 2 introduces the numerical setup, including the host and subhalo models, as well as the initial conditions used in the simulations. The convergence of tidally stripped subhaloes towards an asymptotic remnant is discussed in Section 3.2, the effects of orbital eccentricity in Section 3.3, while the tidal evolution of structural parameters and density profile shape are discussed in Sections 3.4 and 3.5, respectively. The time evolution of bound remnants is discussed in Section 3.6. We describe simple applications of our modelling and compare with earlier work in Section 4. We end with a brief summary of our main conclusions in Section 5. For completeness, numerical convergence issues are discussed in the Appendix.

2 NUMERICAL METHODS

We describe below the numerical setup of the simulations analysed in this work. We assume, for simplicity, that the host halo may be approximated by a static, spherical potential, and that a CDM subhalo may be approximated by an NFW *N*-body model with mass much smaller than the host. We examine orbits that span a range of pericentric radii and eccentricities, and exercise care to monitor and exclude spurious results due to numerical limitations.

2.1 Host halo

The host halo is represented by static, spherical isothermal potential,

$$\Phi_{\rm host}(r) = V_0^2 \, \ln(r/r_0)\,, \tag{1}$$

where $V_0 = 220\,\mathrm{km\,s^{-1}}$ is the circular velocity and r_0 is an arbitrary reference radius. The choice of a static, spherical potential ensures that the subhalo is subject to the same tidal field at each pericentric passage. The corresponding circular velocity profile is flat and is chosen to match approximately the potential inferred for the Milky Way (see e.g. Eilers et al. 2019). The density profile is $\rho_{\rm host}(r) = \rho_0 (r/r_0)^{-2}$ (steeper than that of NFW haloes at the centre; see equation 2), with $V_0^2 = 4\pi G \rho_0 r_0^2$. These parameters correspond to a virial[1] mass, $M_{200} = 3.7 \times 10^{12}\,\mathrm{M_\odot}$, and a virial radius, $r_{200} = 325$ kpc, at redshift $z = 0$.

Although we quote below results for subhaloes in solar masses, kpc, and km s^{-1}, these are only given for illustration and for ease of comparison with Milky Way subhaloes. Gravitational effects are scale free, of course, and our results may be applied to any other value of V_0, or r_0, after proper scaling.

2.2 Orbits

We explore tidal mass-losses of subhaloes on orbits with pericentre-to-apocentre ratios of 1:1, 1:5, 1:10, and 1:20. This eccentricity range includes those derived from *Gaia* proper motions for the orbits of (classical) Milky Way dwarf galaxies (Gaia Collaboration et al. 2018; Fritz et al. 2018) and ultra-faint dwarfs (Simon 2018). All eccentric orbits are chosen to have an apocentric distance of $r_{\rm apo} = 200$ kpc, and the subhaloes are injected at apocentre. The evolution of subhaloes on circular orbits is studied as well, for orbital radii $r = 40$ kpc and $r = 80$ kpc, respectively.

2.3 *N*-body subhaloes

Subhaloes are modelled as *N*-body realizations of the NFW profile,

$$\rho_{\rm NFW}(r) = \frac{\rho_{\rm s}}{(r/r_{\rm s})\,(1 + r/r_{\rm s})^2}\,, \tag{2}$$

where $r_{\rm s}$ is a scale radius and $\rho_{\rm s}$ is a characteristic density. The corresponding circular velocity of this profile peaks at $V_{\rm mx} \approx 1.65\, r_{\rm s}\,(G\rho_{\rm s})^{1/2}$ at a radius $r_{\rm mx} \approx 2.16\, r_{\rm s}$. We shall adopt values measured at $r_{\rm mx}$ as reference parameters in the analysis that follows. At that radius, the circular orbit time, $T_{\rm mx}$, and characteristic mean enclosed density, $\bar{\rho}_{\rm mx}$, may be written as

$$T_{\rm mx} = 2\pi \frac{r_{\rm mx}}{V_{\rm mx}} = \left(\frac{3\pi}{G\bar{\rho}_{\rm mx}}\right)^{1/2}. \tag{3}$$

Similarly, we define the mass $M_{\rm mx} \equiv M(< r_{\rm mx})$ enclosed within $r_{\rm mx}$, and shall hereafter refer to $r_{\rm mx}$, $T_{\rm mx}$, and $M_{\rm mx}$ as the 'characteristic radius', 'characteristic crossing time', and 'characteristic mass' of the subhalo, for short.

The NFW density profile has diverging total mass, so we exponentially truncate the profile outside $10\, r_{\rm s}$. We generate isotropic, equilibrium models by sampling from the corresponding distribution function, obtained through Eddington inversion. We use the implementation described in Errani & Peñarrubia (2020), which is

[1] We define the virial boundary of a halo as the radius where the mean enclosed density equals 200 × the critical density for closure, $\rho_{\rm crit} = 3H_0^2/8\pi G$, with $H_0 = 67\,\mathrm{km\,s^{-1}\,Mpc^{-1}}$ (Planck Collaboration VI 2020). Virial quantities are denoted with '200' subscripts.

available online.[2] Most of our realizations have $N = 10^7$ particles, but we have varied this parameter extensively to check for numerical convergence. See the Appendix for details on numerical convergence tests.

To limit the impact of orbital decay due to tidal mass-losses (see e.g. White 1983; Hernquist & Weinberg 1989, or more recently Fujii, Funato & Makino 2006; Fellhauer & Lin 2007; Miller et al. 2020), we choose an initial subhalo mass, $M_{\rm mx0} \equiv M(< r_{\rm mx0}) = 10^6\,{\rm M}_\odot$, much smaller than the host virial mass, and for which we have verified that the pericentric ($r_{\rm peri}$) and apocentric ($r_{\rm apo}$) distances do not change appreciably even after substantial tidal mass-loss.

We are mainly interested in the regime where considerable tidal mass-loss is expected, so we consider mainly cases where the initial characteristic density of a subhalo does not exceed the mean enclosed density of the host at pericenter. More precisely, we consider mainly cases where the initial characteristic crossing times, $T_{\rm mx0}$, compared with the circular time at pericentre, $T_{\rm peri} = 2\pi r_{\rm peri}/V_0$, satisfies $T_{\rm mx0}/T_{\rm peri} \gtrsim 2/3$. We shall refer to this hereafter as the 'heavy mass-loss regime'. We also report, for completeness, results for models with $T_{\rm mx0}/T_{\rm peri} \lesssim 2/3$ in Section 3.6.3. Overall, we have performed, for each orbit, simulations that span the range of characteristic crossing times, $0.2 < T_{\rm mx}/T_{\rm peri} < 2$.

2.4 Particle-mesh and time integration

We follow the evolution of N-body subhaloes in the tidal field of the host potential using the particle-mesh code SUPERBOX (Fellhauer et al. 2000). This code employs three cubic grids of 128^3 cells each, two of them co-moving with the subhalo and centred on its centre of density. The highest-resolving co-moving grid has a resolution chosen to resolve the subhalo well, with grid size $\Delta x \approx r_{\rm mx0}/128$, where $r_{\rm mx0}$ is the subhalo initial characteristic radius. The second co-moving grid has lower resolution, with grid size ten times larger, $\approx 10\,r_{\rm mx0}/128$. The third grid has grid size $\approx 500\,{\rm kpc}/128$, is fixed in space, and is centred on the host potential.

The time-integration is done using a leapfrog scheme with single and constant time-step $\Delta t = \min(T_{\rm mx0}, T_{\rm peri})/400$. With these choices, a circular orbit at the finest grid resolution ($r \approx r_{\rm mx0}/128$) is resolved with (at least) ≈16 time-steps.

2.5 Self-bound remnant

This study focuses on the properties of self-bound dark matter substructures. We identify bound particles by (i) computing the centre of the subhalo via the shrinking sphere method (Power et al. 2003); (ii) computing the potential and kinetic energy of particles in a reference frame co-moving with the subhalo centre; (iii) discarding unbound particles in the co-moving frame; and iterating until convergence is reached or until the number of bound particles differs by less than one per cent from the previous iteration.

The properties of the self-bound remnant change abruptly as the subhalo passes through pericentre. Therefore, in what follows we choose to measure properties such as remnant density profiles, bound mass fractions, etc., at apocentre, where such properties are less subject to transient effects.

[2] https://github.com/rerrani/nbopy

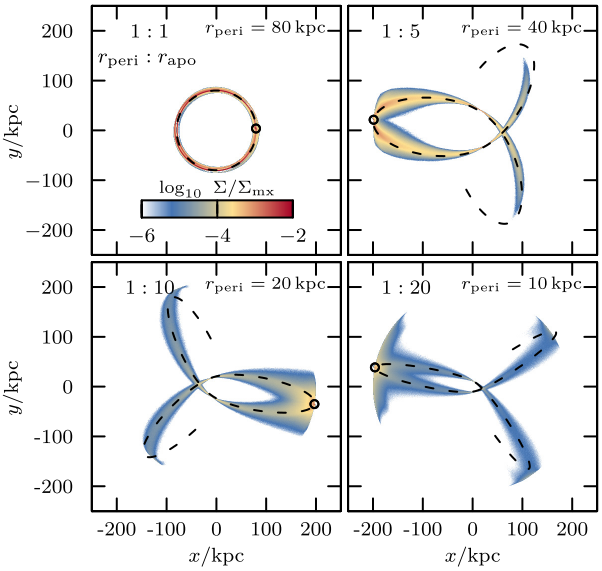

Figure 1. Tidal debris of CDM subhaloes on four different orbits evolved in a spherical, isothermal potential (equation 1). All subhaloes have initial characteristic mass $M_{\rm mx0} = 10^6\,{\rm M}_\odot$, and crossing time $T_{\rm mx0} = 0.9\,T_{\rm peri}$. The snapshots shown correspond to the 20th apocentric passage of each subhalo and show the debris on the orbital plane. The surviving bound remnant position is marked by an open circle. The projected density of tidally stripped material is colour coded, and normalized to the average projected density, $\Sigma_{\rm mx} = M_{\rm mx}/\pi r_{\rm mx}^2$, of the bound remnant. The immediately preceding (and subsequent) orbital path of the remnant is shown by the dashed line in each panel.

3 RESULTS

3.1 General overview

Fig. 1 shows the tidal debris of NFW subhaloes placed on four different orbits of varying eccentricity and pericentric distance. The subhaloes are shown at the 20th apocentric passage, with the immediately preceding (and following) orbital path indicated with dashed lines. The debris clearly stretches along the orbit, as expected for systems where the subhalo mass is negligible compared with the host. The colour scheme has been normalized to the maximum surface density of the bound remnant, which differs substantially from panel to panel because of the varying bound mass fraction of the remnant.

As expected, orbits with smaller pericentres lead to larger mass-loss. This mass-loss appears to continue as the subhalo continues to orbit the host, as shown in Fig. 2, where the bound remnant of one subhalo is shown at various apocentric passages of the evolution for two orbits with the same pericentric distance, $r_{\rm peri} = 40$ kpc. The top row corresponds to a circular orbit while the bottom row corresponds to an orbit with 1:5 pericentre-to-apocentre ratio.

Fig. 2 illustrates a few interesting results. One is that, although for a given pericentre mass-loss progresses faster in the case of a circular orbit (as expected), the remnant is qualitatively indistinguishable from that on the eccentric orbit after approximately the same mass fraction has been lost. Indeed, the circular orbit remnant after 2 orbital periods looks similar to the 1:5 orbit remnant after 10 orbits; in both cases, the bound remnant has retained roughly 6–7 per cent of the initial $M_{\rm mx}$. Ditto for the top-row remnant after five orbits and the bottom-row remnant after 20 orbits, when the bound remnant has been reduced in both cases to ∼2–3 per cent of the initial mass.

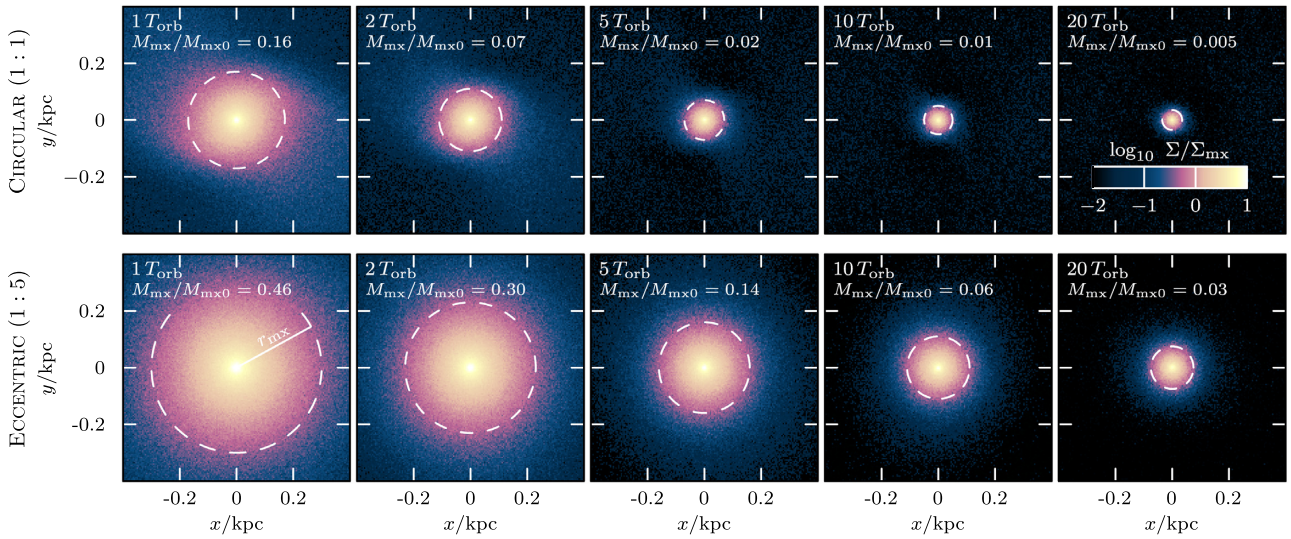

Figure 2. Projected structure of two bound remnants at various stages of their tidal evolution. The top row shows the projected densities of a subhalo on a circular orbit with $r = 40$ kpc in an isothermal potential after 1, 2, . . . , 20 orbital periods. The subhalo has an initial characteristic mass $M_{\rm mx0} = 10^6\,{\rm M}_\odot$ and crossing time $T_{\rm mx0} = 0.88\,T_{\rm peri}$, i.e. an initial characteristic radius and circular velocity of $r_{\rm mx0} = 0.48$ kpc and $V_{\rm mx0} = 3.0\,{\rm km\,s^{-1}}$, respectively. The bound mass fraction is listed in the legend of each panel. The bottom row shows the same subhalo on an eccentric orbit with $r_{\rm peri} = 40$ kpc and $r_{\rm apo} = 200$ kpc. It takes considerably longer to strip the subhalo on the eccentric orbit compared to the circular case. The projected density (normalized to the average projected density of the bound remnant, $\Sigma_{\rm mx} = M_{\rm mx}/\pi r_{\rm mx}^2$) is colour coded.

The second point to note from Fig. 2 is that, although mass-loss is continuous, it slows down as the evolution progresses. For example, the eccentric-orbit subhalo takes only ∼1 orbit to lose half of its mass at the beginning, but takes ∼10 orbits to reduce its bound mass by the same factor between 10 and 20 $T_{\rm orb}$. This suggests that a subhalo on an orbit with fixed pericenter is stripped until it converges to a well-defined self-bound 'asymptotic tidal remnant'. We explore this idea further below.

3.2 Asymptotic tidal remnants

The effects of tidal mass-loss are easily appreciated in Fig. 3, where we show the circular velocity profiles of two subhaloes, placed on circular orbits with $r = 40$ kpc (left) and $r = 80$ kpc (right). The subhalo on the 40 kpc orbit is the one shown previously in the top panel of Fig. 2 with a ratio of crossing times of $T_{\rm mx0}/T_{\rm peri} = 0.88$, while the subhalo on the 80 kpc orbit has $T_{\rm mx0}/T_{\rm peri} = 2/3$. Curves are spaced by one orbital period, and each curve is normalized to the initial values of $r_{\rm mx}$ and $V_{\rm mx}$, which are $\{0.48\,{\rm kpc}, 3.0\,{\rm km\,s^{-1}}\}$ and $\{0.63\,{\rm kpc},\ 2.6\,{\rm km\,s^{-1}}\}$ for the subhalo on the 40 and 80 kpc orbits, respectively.

The gradual convergence to a well-defined asymptotic remnant structure is quite clear; after ∼10 orbits there is little further change in the mass profile of the remnant. The final characteristic density appears set by the mean density of the host at pericentre: more precisely, the subhalo is stripped gradually until its characteristic crossing time approaches a fixed fraction of the circular time at pericentre; $T_{\rm mx} \approx T_{\rm peri}/4$, or, equivalently, until its characteristic density is ∼16 × the mean host density at pericentre. This is a general result of our simulations in the heavy mass-loss regime.

We illustrate this in Fig. 4, which shows the evolution of the characteristic crossing time of subhaloes in circular orbit at two different radii from the centre of the host: 40 kpc (red) and 80 (blue) kpc, respectively. Each curve corresponds to subhaloes with different initial characteristic densities, and follows a system for 20 orbital times, or until its $M_{\rm mx}$ has been reduced to about 0.3 per cent of its initial value, when numerical limitations begin to dominate (see the Appendix). This mass reduction is equivalent to a reduction of nearly ∼16 in the initial $r_{\rm mx}$ or, alternatively, a factor of ∼5 in $V_{\rm mx}$ or ∼3 in $T_{\rm mx}$.

As is clear from Fig. 4, all subhaloes are stripped until their characteristic crossing times are reduced to $T_{\rm mx} \approx T_{\rm peri}/4$, independent of the initial properties of the subhalo. This is true of all our runs in the 'heavy mass-loss regime', where the initial characteristic density of the subhalo is low compared with the host density at pericenter (or, more precisely, when $T_{\rm mx0}/T_{\rm peri} > 2/3$).

For comparison, we have computed characteristic crossing times of selected subhaloes on circular orbits in the public DASH simulation suite (Ogiya et al. 2019), and observe that also there, tidal evolution decelerates, consistent with an evolution towards an asymptotic remnant.

3.3 The effect of orbital eccentricity

Circular orbits are rare in a cosmological setting, so it is important to explore how the results discussed above are modified for subhaloes on eccentric orbits. As hinted at when discussing Fig. 2, for given pericentre, tides are expected to operate on a longer time-scale for eccentric orbits, mainly because tidal forces are strongest during pericentric passage and subhaloes spend less time near pericentre the more eccentric the orbit. Is the tidal evolution on highly eccentric orbits just delayed, but otherwise similar to that on circular orbits?

We see that this is indeed the case in Fig. 5, where we show the evolution of $T_{\rm mx}$ for a subhalo on four orbits with the same pericentre but different eccentricities. The subhalo has, initially, $T_{\rm mx0} = (2/3)\,T_{\rm peri}$. The filled blue circles correspond to a subhalo that evolves on a circular orbit. Open circles correspond to results for other orbital eccentricities, after scaling each in time by a factor, $f_{\rm ecc} = 5$, 6.5, and 8 for orbits with pericentre-to-apocentre ratios of 1:5, 1:10, and 1:20, respectively. The excellent agreement between

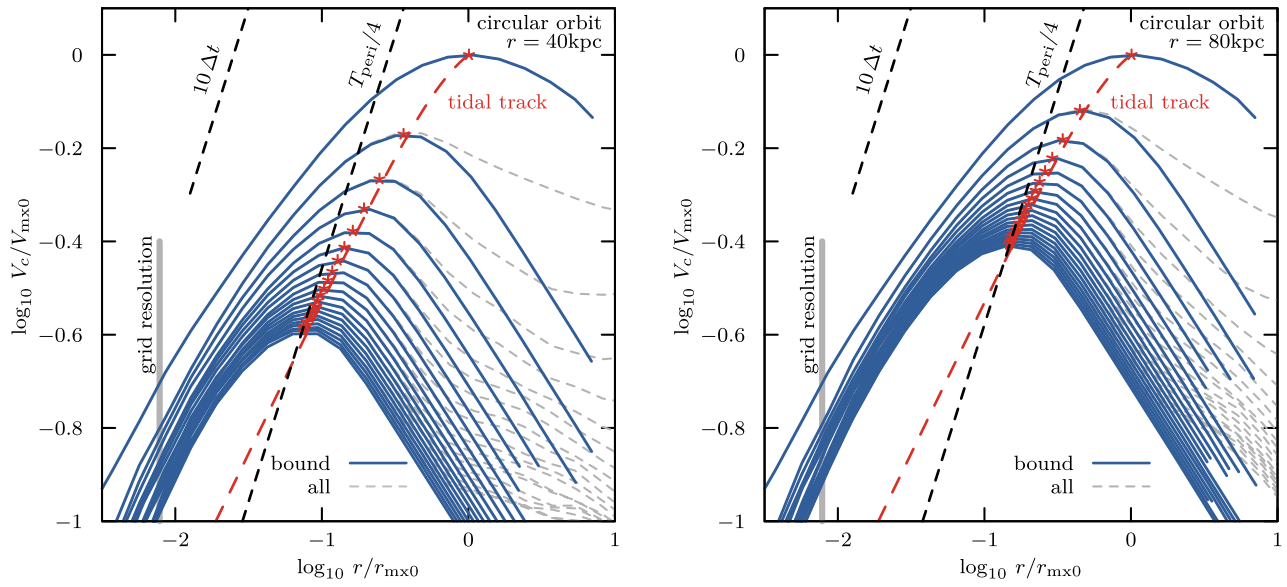

Figure 3. Circular velocity profiles of the bound remnants of two subhaloes on circular orbits, normalized to their initial characteristic radius and velocity. Grey curves correspond to all subhalo mass, blue curves to the self-bound remnant. Curves are spaced by one orbital period, for a total of 20 orbital periods. The left-hand panel shows the evolution of the same subhalo as in the top panel of Fig. 2 ($r_{\rm mx0} = 0.48$ kpc, $V_{\rm mx0} = 3.0\,{\rm km\,s^{-1}}$) on an orbit with $r = 40$ kpc and $T_{\rm mx0}/T_{\rm peri} = 0.88$. The right panel shows a different subhalo ($r_{\rm mx0} = 0.63$ kpc, $V_{\rm mx0} = 2.6\,{\rm km\,s^{-1}}$) on an orbit with $r = 80$ kpc, which implies $T_{\rm mx0}/T_{\rm peri} = 2/3$ (for circular orbits $T_{\rm peri} = T_{\rm orb}$). The evolution of $\{r_{\rm mx}, V_{\rm mx}\}$ follows well-defined *tidal tracks* (red dashed curves), which we discuss further in Section 3.4. In both cases, the evolution of the remnant slows down as $T_{\rm mx}$ approaches $T_{\rm peri}/4$. The final structure of a subhalo in the heavy mass-loss regime (i.e. $T_{\rm mx0}/T_{\rm peri} > 2/3$) is set solely by the properties of the host at pericentre.

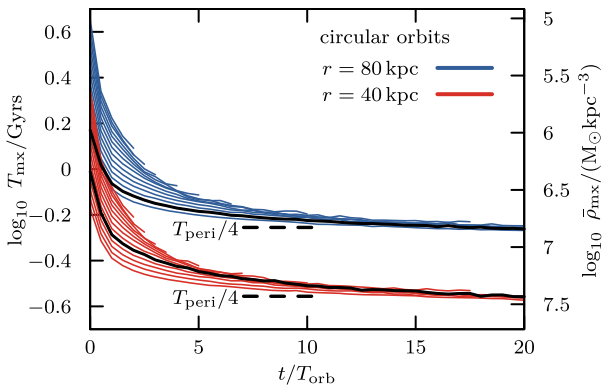

Figure 4. Evolution of the characteristic crossing time, $T_{\rm mx}$, of subhaloes on circular orbits with two different radii; $r = 40$ kpc (red curves) and $r = 80$ kpc (blue curves). Black curves highlight the two cases shown in Fig. 3. All subhaloes are in the heavy mass-loss regime, with initial crossing times in the range $2/3 < T_{\rm mx0}/T_{\rm peri} < 2$, where $T_{\rm peri} = T_{\rm orb}$ for circular orbits. Subhaloes are followed until their structure becomes compromised by numerical limitations, which become manifest when $T_{\rm mx}$ has been reduced to less than $\sim$1/3 of its initial value for our 10^7 –particle realizations. See the Appendix for further discussion on numerical convergence. All subhaloes are seen to approach an asymptotic value of $T_{\rm mx}$ set solely by the host properties at the orbital pericentre.

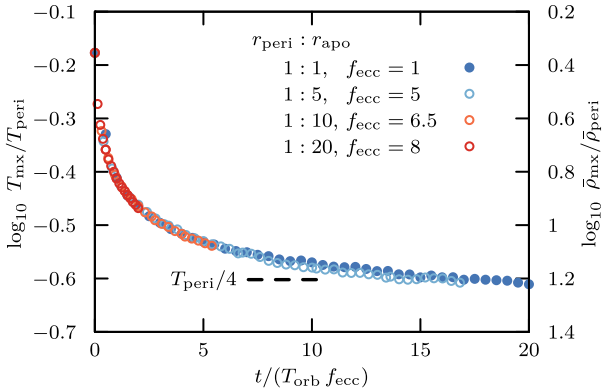

Figure 5. Evolution of the characteristic crossing time, $T_{\rm mx}$, (or, equivalently, of the characteristic density, scale on right) of a subhalo placed on orbits with fixed pericentric distance and varying eccentricities with pericentre-to-apocentre ratios 1:1, 1:5, 1:10, and 1:20. The evolution is similar in all cases, but occurs on longer time-scales with increasing orbital eccentricity. At equal pericentre, the main effect of orbital eccentricity is to 'delay' the tidal evolution of a subhalo. All subhaloes evolve in the same way after scaling times by an eccentricity-dependent factor $f_{\rm ecc}$, listed in the legend. For example, it takes $f_{\rm ecc} = 8$ times longer for a subhalo to be stripped to the same extent on a 1:20 orbit than on a circular orbit with the same pericentric radius.

the various curves confirms that the main effect of orbital eccentricity is simply a 'delay'.

In other words, it takes five times more orbits for a subhalo on a 1:5 orbit to evolve to the same stage as a subhalo on a circular orbit. Longer delays accompany higher eccentricities, but the delay factor appears to nearly saturate for eccentricities as high as 1:10 or 1:20, the highest value explored in our runs. We find that this is also a general result of our runs: all results obtained for circular orbits are generally applicable to other eccentricities simply by scaling time by the appropriate factor $f_{\rm ecc}$.

The following function may be used to interpolate between our four measured values of $f_{\rm ecc}$ for a given apocentre-to-pericentre ratio:

$$f_{\rm ecc} \approx [2x/(x+1)]^{3.2} \quad \text{where } x = r_{\rm apo}/r_{\rm peri}\,. \tag{4}$$

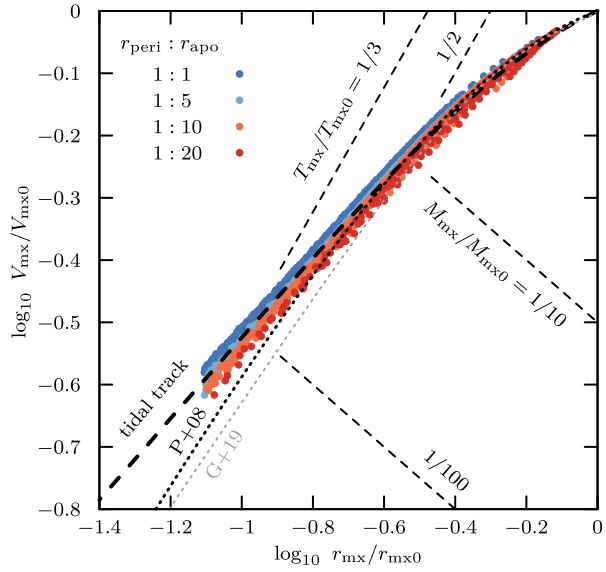

Figure 6. Subhalo structural parameters ($r_{\rm mx}$, $V_{\rm mx}$, normalized to their initial values) evolve along a well-defined *tidal track* that is nearly independent of orbital eccentricity. Filled circles correspond to measurements for *all* of our well-resolved N-body models, while the dashed black curve shows the fit given by equation (5). Constant remnant mass fractions, $M_{\rm mx}/M_{\rm mx0}$, and constant crossing time fractions, $T_{\rm mx}/T_{\rm mx0}$, are shown by black dashed lines. The original tidal track of Peñarrubia et al. (2008) is shown by the black dotted curve, while the tracks of Green & van den Bosch (2019) for subhaloes of concentration $c = r_{200}/r_{\rm s} = 10$ are shown by a grey dotted curve.

A fitted exponent of ≈3.2 reproduces the measured factors $f_{\rm ecc}$ at their respective ratios of $r_{\rm apo}/r_{\rm peri}$ within 5 per cent.

Note that these factors are measured from simulated subhaloes on orbits in an isothermal potential approximating the Milky Way (equation 1). These factors may take slightly different numerical values in potentials with a substantially different radial dependence of the tidal forces.

We emphasize again that, while more pericentric passages are needed for a subhalo on an eccentric orbit to be tidally stripped to the same extent as on a circular orbit, the characteristic crossing time (density) of the asymptotic remnant (in the 'heavy mass-loss regime') is independent of orbital eccentricity and appears set solely by the circular time (density) of the host halo at pericentre.

3.4 Tidal evolutionary tracks

As may be seen in Fig. 3, the structural parameters $r_{\rm mx}$ and $V_{\rm mx}$ of the subhaloes evolve along clearly defined 'paths', indicated by the dashed red line in each panel. This is consistent with earlier work, which has shown that, as subhaloes lose mass to tides, their characteristic parameters evolve along well-defined 'tidal tracks'. The position along the track depends only on the total amount of mass lost, and is largely independent of the eccentricity of the orbit and/or of the elapsed number of orbits. This was first discussed in Peñarrubia et al. 2008, hereafter $P + 08$ (and confirmed in later work; see e.g. Green & van den Bosch 2019).

We explore this further in Fig. 6, where we show, for all of our runs, the evolution of the subhalo structural parameters $\{r_{\rm mx}, V_{\rm mx}\}$, normalized to their initial values $\{r_{\rm mx0}, V_{\rm mx0}\}$, and coloured by the eccentricity of the orbit. It is clear that a unique track describes well all runs, which may be parametrized by a simple function,

$$V_{\rm mx}/V_{\rm mx0} = 2^{\alpha}\ (r_{\rm mx}/r_{\rm mx0})^{\beta}\ \left[1 + (r_{\rm mx}/r_{\rm mx0})^{2}\right]^{-\alpha}\ , \tag{5}$$

with $\alpha = 0.4$, $\beta = 0.65$. Note that this parametrization is slightly different from the one proposed by P + 08 (shown with a black dotted line), an update made possible by the higher numerical resolution of our present runs, which give robust results for subhaloes that retain as little as 0.3 per cent of their initial characteristic mass, $M_{\rm mx}$.

An interesting feature of the tidal track is its clear curvature for modest mass-losses (i.e. for $r_{\rm mx}/r_{\rm mx0} > 1/3$, or $M_{\rm mx}/M_{\rm mx0} > 0.1$) and a power-law behaviour for heavier mass-losses ($M_{\rm mx}/M_{\rm mx0} < 0.1$), where the relation becomes

$$V_{\rm mx}/V_{\rm mx0} \propto (r_{\rm mx}/r_{\rm mx0})^{0.65}, \tag{6}$$

consistent with the power-law fits in Errani & Peñarrubia (2020). As we discuss below, the reason for this change is that heavily stripped NFW haloes converge to a new mass profile shape after substantial tidal mass-loss. The curvature in the tidal track corresponds to the transition from the initial NFW mass profile to the new profile; once this is established further mass-loss is 'self-similar' and results in a simple power-law scaling between $r_{\rm mx}$ and $V_{\rm mx}$.

We emphasize again that the tidal track in Fig. 6 applies equally well to *all* of our runs, regardless of pericentric radii and/or orbital eccentricity. This is true *provided* that the remnant can be adequately resolved. As we discuss in the Appendix, poor numerical resolution leads to systematic deviations from the tidal track, usually towards artificially low values of $V_{\rm mx}$ and/or artificially large values of $r_{\rm mx}$. These deviations result in characteristic crossing times longer than those of well-resolved subhaloes, making the poorly resolved remnants prone to further tidal mass-loss and eventual disruption. In what follows, we shall focus only on well-resolved systems, which we may define as those whose characteristic crossing times, $T_{\rm mx}$, deviate by less than 10 per cent from the tidal track given by equation 5. See the Appendix for further discussion.

3.5 Evolution of the density profile

As subhaloes lose mass to tides, the shape of their mass profiles evolves from the original NFW shape adopted as initial conditions, and approaches a different profile shape after substantial mass-loss has occurred. We show this in Fig. 7, where the left-hand panel shows the circular velocity profiles of a number of subhaloes on 1:5 eccentric orbits, coloured by their remaining bound mass fraction, and scaled to their *current* values of $r_{\rm mx}$ and $V_{\rm mx}$. Similar results are obtained for all types of orbits; we choose here subhaloes on 1:5 orbits only as illustration.

The NFW profile is shown in Fig. 7 by the solid black line, and it agrees, by construction, with the initial subhalo profile (red curve). As a subhalo loses mass, the V_c profile of its bound remnant becomes noticeably 'narrower', with less mass in the outer regions, but also less mass in the regions inside $r_{\rm mx}$ relative to the initial NFW profile. Gradually, this profile approaches a new asymptotic shape, which we indicate with the dashed black curve in Fig. 7.

The transition from the initial NFW density profile (equation 2) to the asymptotic shape may be described by an exponential truncation of the initial profile, as follows:

$$\rho(r) = \rho_{\rm NFW}(r)\ \times\ \exp(-r/r_{\rm cut})\ /\ (1 + r_{\rm s}/r_{\rm cut})^{\kappa}, \tag{7}$$

where $r_{\rm s}$ denotes the scale radius of the initial NFW profile, and $\kappa = 0.3$ is chosen to match the 'tidal track' evolution discussed above in Section 3.4. For $r_{\rm cut}/r_{\rm s} \to \infty$, this description recovers the initial

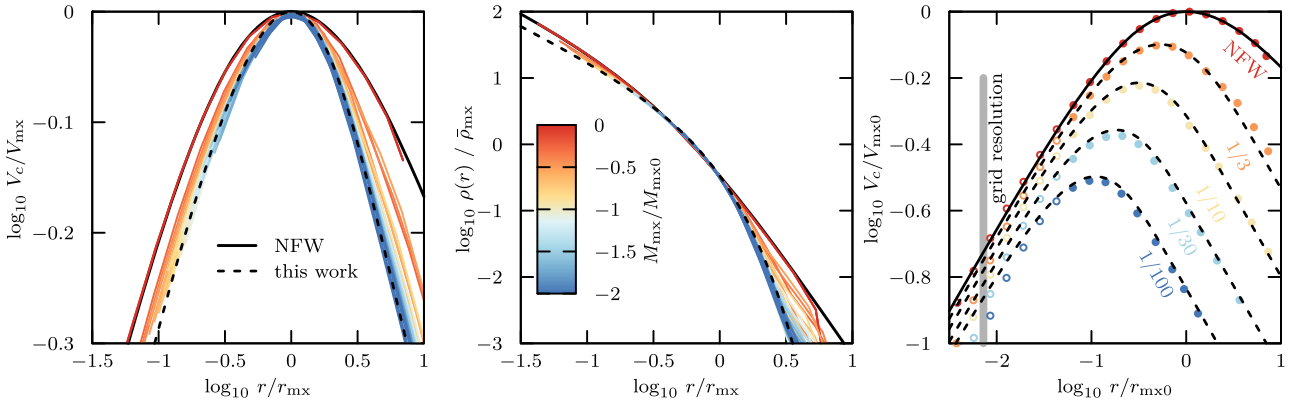

Figure 7. Mass profiles of stripped NFW subhaloes. The left-hand panel shows circular velocity profiles, normalized to their current values of $r_{\rm mx}$ and $V_{\rm mx}$, and coloured by the remaining self-bound mass fraction of the remnant (see colour bar in middle panel). The middle panel shows the density profiles of the same subhaloes, normalized in a similar manner. Both of these panels show that the structure of a heavily stripped NFW subhalo approaches a new, exponentially truncated density profile whose shape is well approximated by equation (7). The right-hand panel shows circular velocity curves for selected simulation snapshots at remnant bound masses of $M_{\rm mx}/M_{\rm mx0} = 1, \ldots, 1/100$ scaled to the initial values $\{r_{\rm mx0}, V_{\rm mx0}\}$. Radii at which the circular velocity may be affected by resolution limitations according to the criteria of the Appendix are shown using open circles, while filled circles correspond to radii unaffected by resolution. Exponentially truncated NFW profiles, with truncation radii $r_{\rm cut}$ selected to match the measured $M_{\rm mx}$ (see Fig. 8), are shown using black dashed curves.

NFW profile, whereas for $r_{\rm cut}/r_{\rm s} \to 0$, the density profile converges to an exponentially truncated cusp.

For heavy mass-losses, i.e. $r_{\rm cut}/r_{\rm s} \to 0$, equation (7) reduces to an exponentially truncated cusp,

$$\rho_{\rm asy}(r) = \rho_{\rm cut}\,(r/r_{\rm cut})^{-1}\,\exp(-r/r_{\rm cut})\,, \tag{8}$$

where $\rho_{\rm cut} = \rho_{\rm s}\,(r_{\rm cut}/r_{\rm s})^{\kappa-1}$, and $r_{\rm s}$ and $\rho_{\rm s}$ denote the scale radius and scale density of the initial NFW profile, respectively. The asymptotic profile of equation (8) has a convergent total mass of $M_{\rm tot} = 4\pi r_{\rm cut}^3 \rho_{\rm cut}$, and a circular velocity curve which peaks at a radius $r_{\rm mx} \approx 1.8\,r_{\rm cut}$ with a characteristic mass of $M_{\rm mx} \approx 0.5\,M_{\rm tot}$. Consequently, this profile is consistent with the power-law tidal tracks $V_{\rm mx} \propto r_{\rm mx}^{\beta}$, where $\beta = (1+\kappa)/2 \approx 0.65$ for a value of $\kappa \approx 0.3$.

For intermediate amounts of mass-loss equation (7) describes well the profile of the remnant, with a value of $r_{\rm cut}/r_s$ that depends only on the current bound mass fraction. While the relation of truncation radius $r_{\rm cut}$ and remnant bound mass $M_{\rm mx}$ follows directly from integrating equation (7), we present for ease of use the following fit, which reproduces well the relation shown in Fig. 8 (and is consistent with our simulations for the resolved range of remnant masses, $M_{\rm mx}/M_{\rm mx0} \gtrsim 1/300$):

$$\frac{r_{\rm cut}}{r_{\rm mx0}} \approx 0.44 \times \left(\frac{M_{\rm mx}}{M_{\rm mx0}}\right)^{0.44} \left[1 - \left(\frac{M_{\rm mx}}{M_{\rm mx0}}\right)^{0.3}\right]^{-1.1}. \tag{9}$$

Here, $r_{\rm mx0} \approx 2.16\,r_{\rm s}$ is the characteristic radius of the initial NFW profile. The functional form of equation (9) ensures that (i) for $M_{\rm mx}/M_{\rm mx0} \to 1$, $r_{\rm cut}/r_{\rm mx0} \to \infty$, i.e. the profile prior to mass-loss is an NFW profile, and (ii) for $M_{\rm mx}/M_{\rm mx0} \to 0$, the correct asymptotic bound mass of equation (8) is recovered.[3] The right-hand panel of Fig. 7 compares the results of this fitting formula with the profiles of simulated subhaloes spanning two decades in mass-loss, with excellent results.

[3]In the asymptotic regime, integrating equation (8) with $\rho_{\rm cut} = \rho_{\rm s}\,(r_{\rm cut}/r_{\rm s})^{\kappa-1}$ and $r_{\rm s} \approx r_{\rm mx0}/2.16$ yields $r_{\rm cut}/r_{\rm mx0} \propto (M_{\rm mx}/M_{\rm mx0})^{1/(2+\kappa)}$ with exponent $1/(2+\kappa) \approx 0.44$.

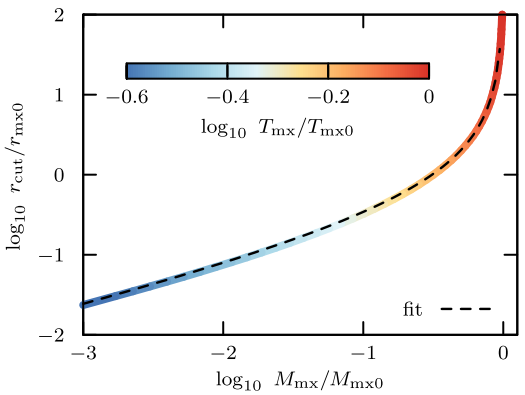

Figure 8. For the tidally truncated profile of Fig. 7 (see equation 7), the truncation radius $r_{\rm cut}$ follows directly from the remnant bound mass fraction, $M_{\rm mx}/M_{\rm mx0}$. A truncation radius of $r_{\rm cut}/r_{\rm mx0} \to \infty$ recovers NFW, while for $r_{\rm cut}/r_{\rm mx0} \to 0$, the profile converges to an exponentially truncated cusp. While the relation of $M_{\rm mx}/M_{\rm mx0}$ and $r_{\rm cut}/r_{\rm mx0}$ follows directly from equation (7), the dashed curve (equation 9) provides a simple fit for ease of use.

The model of equation (7) may be directly compared to that of Green & van den Bosch (2019, hereafter G + 19), who propose a 'transfer function', $\rho/\rho_{\rm NFW}$, to model the structural changes to NFW profiles during tidal evolution, fitted to simulation snapshots of the DASH simulation series (Ogiya et al. 2019) . The transfer function corresponding to equation (7) is compared in Fig. 9 to that of G + 19. Note that our model leads to higher central densities at equal fractions of remnant bound mass $M_{\rm mx}/M_{\rm mx0}$. The main difference lies in the normalization of the density profile, and not in its shape, as shown by the gradual divergence in the G + 19 tidal track from ours seen in Fig. 6. Note, however, that even for the most highly stripped subhalo considered 'resolved' in this work ($M_{\rm mx}/M_{\rm mx0} \sim 1/300$), the differences are rather small. Indeed, the G + 19 track differs from ours there by less than 0.1 dex in $V_{\rm mx}$, or, equivalently, by less than 0.2 dex in $r_{\rm mx}$.

We turn our attention now to the time evolution of the characteristic parameters of the profile. Since the characteristic radius ($r_{\rm mx}$) and ve-

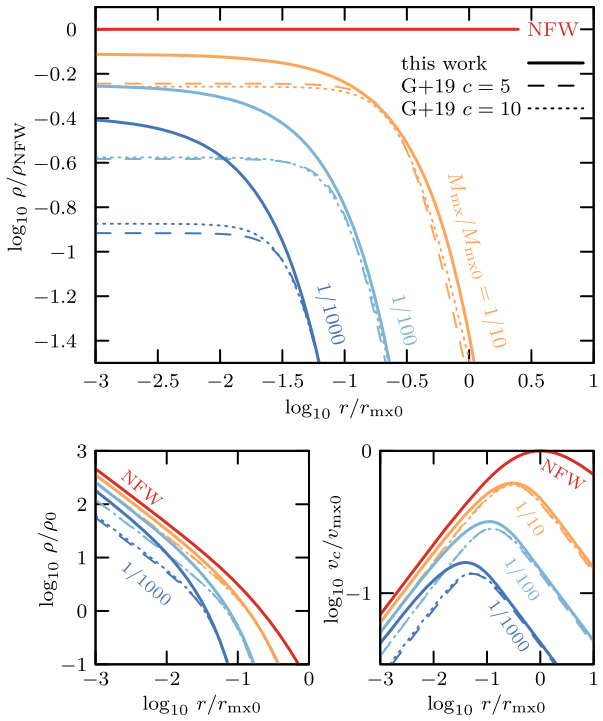

Figure 9. Transfer function $\rho/\rho_{\rm NFW}$ (top panel) as well as density profiles (bottom left) and circular velocity curves (bottom right) of the model of equation (7) for different fractions of bound mass $M_{\rm mx}/M_{\rm mx0}$. The model of equation (7) ('this work', solid lines) is compared against the Green & van den Bosch (2019) model for initial subhalo concentrations $c = r_{200}/r_{\rm s} = 5$ ('G + 19', dotted lines) and 10 (dashed lines). Note that the model of equation (7) predicts higher central densities at equal bound mass fraction, and results in tidal tracks with a different asymptotic slope (see Fig. 6).

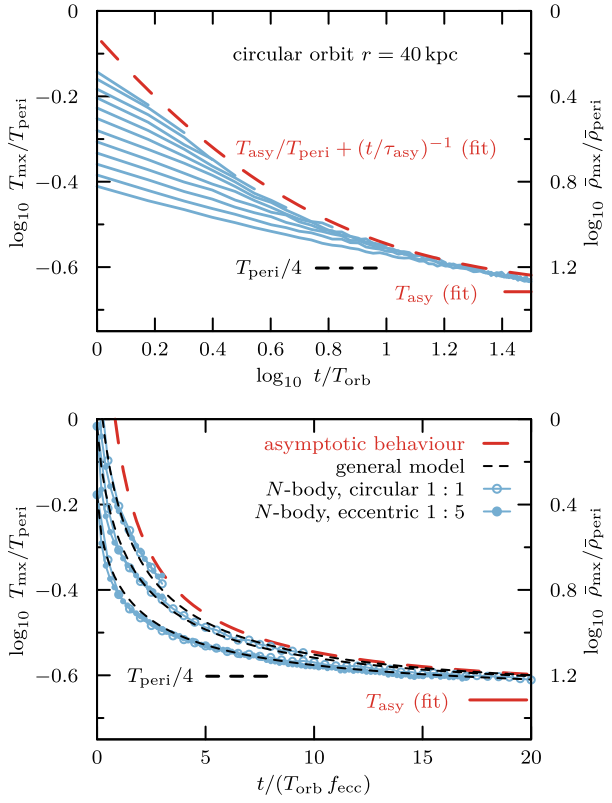

Figure 10. *Top:* Time evolution of the characteristic crossing time of subhaloes on circular orbits in the heavy mass-loss regime. The evolution is shown in logarithmic units for a number of subhaloes with initial crossing times of $T_{\rm mx0}/T_{\rm peri} > 2/3$ in order to highlight the long-term behaviour of the subhaloes, all of which approach at late times the same asymptotic power-law trend, highlighted by the red dashed curve and parametrized by equation (10). Short horizontal segments indicate the value of $T_{\rm mx}$ to which bound remnants converge in our simulations, $T_{\rm peri}/4$, which differs slightly from the fitted 'true asymptotic' value (i.e. applicable for $t = \infty$), $T_{\rm asy} \approx 0.22\, T_{\rm peri}$. *Bottom:* Results for three subhaloes of different initial, $T_{\rm mx0}/T_{\rm peri}$, placed on different orbits and compared with the empirical model parametrized by equation (12). Circular orbits are shown with open circles; filled circles correspond to 1: 5 eccentric orbits with the same pericentric radius. Eccentric orbit times have been scaled by $f_{\rm ecc} = 5$, as discussed in Section 3.3. Aside from this delay, equation (12) describes very well the results of all simulations.

locity ($V_{\rm mx}$) are linked by the tidal track shown in Fig. 6 (equation 5), we only need to consider the evolution of one characteristic structural parameter to describe the full evolution. We choose the crossing time, $T_{\rm mx}$, for this exercise next.

3.6 Time evolution

We explore next how subhaloes approach the asymptotic remnant stage as a function of time. This is illustrated in the top panel of Fig. 10, which shows the evolution of $T_{\rm mx}$ as a function of time for subhaloes on circular orbits at $r = 40$ kpc from the centre of the host. Times are scaled to the orbital time, $T_{\rm orb}$, and $T_{\rm mx}$ is shown in units of the host circular time at pericentre, $T_{\rm peri}$. Although, of course, $T_{\rm orb} = T_{\rm peri}$ for circular orbits, this choice of scaling is useful, as it will enable us to extend the comparison to eccentric orbits, where the orbital time can be much longer than $T_{\rm peri}$. We consider first only subhaloes in the heavy mass-loss regime, i.e. $T_{\rm mx0}/T_{\rm peri} > 2/3$.

The top panel of Fig. 10 shows that all subhaloes approach the same asymptotic remnant value, $T_{\rm asy}$. As discussed in Section 3.5, one may identify two phases in the evolution, one that applies to early times, when the subhalo mass profile shape changes rapidly from NFW-like to a new shape, and another one as all subhaloes approach the same asymptotic remnant stage. During the first stage subhaloes with larger values of $T_{\rm mx0}/T_{\rm peri}$ evolve more rapidly, but they all seem to approach the same asymptotic behaviour after roughly ∼10 orbits.

3.6.1 *Heavy mass-loss regime: late asymptotic behaviour*

The asymptotic behaviour may be approximated by a simple power law (red dashed line in Fig. 10),

$$Y_{\rm asy}(t) \equiv (T_{\rm mx}(t) - T_{\rm asy})/T_{\rm peri} = (t/\tau_{\rm asy})^{-1}. \quad (10)$$

With $T_{\rm asy} \approx 0.22\, T_{\rm peri}$ and $\tau_{\rm asy} \approx 0.65\, T_{\rm orb}$, this equation describes well the late stages of all of our runs in the heavy mass-loss regime. This power law is the solution to the differential equation

$$\mathrm{d}Y_{\rm asy}(t)/\mathrm{d}t = -Y_{\rm asy}^2(t)/\tau_{\rm asy}, \quad (11)$$

hence the asymptotic evolution of a subhalo's crossing time is such that the slope $\mathrm{d}Y_{\rm asy}(t)/\mathrm{d}t$ depends on the instantaneous value of $Y_{\rm asy}(t)$ alone, consistent with the observation that the subhalo profile shape converges: once the profile shape has converged, the subhalo structure is fully determined by the single parameter $T_{\rm mx}(t)$. This late evolution may be thought of as 'self-similar' in the sense that it is independent of the initial conditions, and progresses at a rate governed only by the instantaneous value of $T_{\rm mx} - T_{\rm asy}$.

3.6.2 Heavy mass-loss regime: general description

The early evolution deviates from the asymptotic power-law behaviour discussed above. The following empirical formula describes well the general evolution in the heavy mass-loss regime:

$$Y(t) = (T_{\rm mx}(t) - T_{\rm asy})/T_{\rm peri} = Y_0\,[1 + (t/\tau)^{\eta}]^{-1/\eta}, \quad (12)$$

where $Y_0 = (T_{\rm mx0} - T_{\rm asy})/T_{\rm peri}$ is determined by the initial conditions, and η is a free parameter that may be inferred from the simulation results.

With this parametrization, the fact that all subhaloes in Fig. 10 approach the *same* late evolution implies that the time-scale τ is inversely proportional to Y_0, i.e.

$$\tau = \tau_{\rm asy}/Y_0. \quad (13)$$

Least-squares fits to the simulation data show that $\eta \lesssim 1$, and that η correlates with Y_0, within ten per cent of the following empirical function:

$$\eta \approx 1 - \exp(-2.5\,Y_0)\,. \quad (14)$$

The bottom panel of Fig. 10 compares fits using equation (12) with simulation results. For clarity, we show only three different subhaloes on circular orbits (open circles), but include also the results for orbits with 1:5 pericentre-to-apocentre ratio (filled circles). As expected from our discussion in Section 3.3, open and filled circles overlap after the eccentric orbital times are scaled by $f_{\rm ecc} = 5$. Aside from this eccentricity-dependent 'delay', equation (12) describes well the overall evolution of all runs, regardless of orbital eccentricity.

A simple implementation of this model for the tidal evolution of subhaloes is made available online.[4] The implementation takes as inputs the initial subhalo structural parameters $\{r_{\rm mx0}, V_{\rm mx0}\}$ as well as host halo crossing time $T_{\rm peri}$ at pericentre, orbital period $T_{\rm orb}$ and pericentre-to-apocentre ratio, and returns the time evolution of the subhalo structural parameters $\{r_{\rm mx}(t), V_{\rm mx}(t)\}$.

3.6.3 Modest mass-loss regime

Subhaloes with characteristic densities substantially higher than the host density at the pericentre of their orbits will be only modestly affected by tides. In this regime (i.e. when $T_{\rm mx0}/T_{\rm peri} < 2/3$), the remnant is *not* expected to have the same characteristic density as the asymptotic tidal remnant discussed in the preceding subsection. Their characteristic densities must somehow in this case reflect their initial values.

Fig. 11 shows the evolution of $T_{\rm mx}$ for subhaloes on circular orbits with $r = 80$ kpc, and $0.2 < T_{\rm mx0}/T_{\rm peri} < 2$. The evolution of subhaloes with $T_{\rm mx0}/T_{\rm peri} > 2/3$ (i.e. in the heavy mass-loss regime or 'regime I', shown with blue curves) are analogous to those discussed above, and are seen to approach remnants with the same asymptotic crossing time, $\sim T_{\rm peri}/4$.

On the other hand, subhaloes with $T_{\rm mx0}/T_{\rm peri} < 2/3$ are shown using red curves. Tidal effects on these haloes are modest, and the evolution of $T_{\rm mx}$ quickly stalls after a few orbits. After 20 full circular orbital periods the remnants have not yet settled to a final value, but evolve only weakly thereafter.

We may fit the tidal evolution of these subhaloes using the same equation (12), with 'primes' to distinguish parameters specific to the modest mass-loss regime ('regime II'):

$$Y'(t) = Y'_0\,\left[1 + (t/\tau')^{\eta'}\right]^{-1/\eta'}, \quad (15)$$

[4] https://github.com/rerrani/tipy

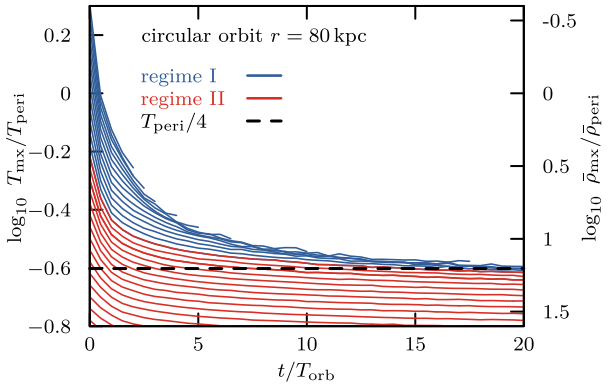

Figure 11. As Fig. 10, but for circular orbits with $r = 80$ kpc, and spanning a wide range of $T_{\rm mx0}/T_{\rm peri}$. Haloes in the heavy mass-loss 'regime I' (i.e. $T_{\rm mx0}/T_{\rm peri} > 2/3$) are shown in blue, those in the modest mass-loss 'regime II' (i.e. $T_{\rm mx0}/T_{\rm peri} < 2/3$) are shown in red. In regime I, all haloes converge to remnants with the same asymptotic value of $T_{\rm mx} \approx T_{\rm peri}/4$. In regime II, haloes approach a remnant whose characteristic crossing time (density) depends on their initial value. Most subhaloes in a cosmological context fall in regime I (see Section 3.2 for details).

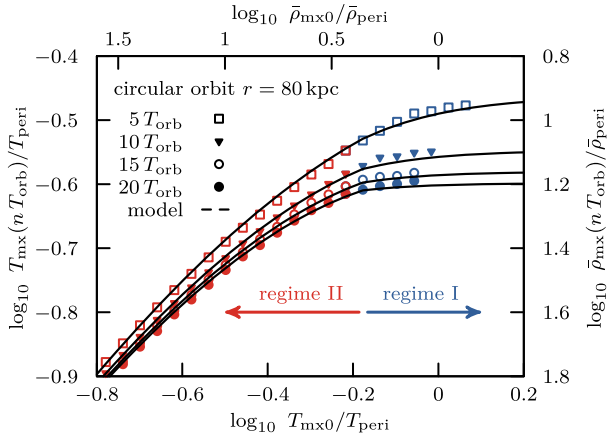

Figure 12. Crossing times of subhaloes after $n = 5$, 10, 15, and 20 orbital times. The characteristic densities of subhaloes in regime I (i.e. $T_{\rm mx0}/T_{\rm peri} > 2/3$) converge to an asymptotic value that is set solely by $T_{\rm peri}$ and is independent of the initial value $T_{\rm mx0}$. Those in regime II (i.e. $T_{\rm mx0}/T_{\rm peri} < 2/3$) converge to characteristic densities that reflect their initial values. Solid black curves show the empirical results from equation (15) for regime II, and from equation (12) for regime I.

where $Y' = (T_{\rm mx} - T'_{\rm asy})/T_{\rm peri}$. The exponent $\eta' = 0.67$ may be fixed by requiring that it should be identical to the exponent of equation (12) at the boundary between regimes I and II. The main difference from the previous results is that, in regime II, the 'asymptotic' crossing time $T'_{\rm asy}$ depends on the initial $T_{\rm mx0}$ of the subhalo, and not solely on $T_{\rm peri}$. We estimate $T'_{\rm asy}$ through the following empirical function,

$$T'_{\rm asy}/T_{\rm peri} = \frac{T_{\rm mx0}/T_{\rm peri}}{(1 + T_{\rm mx0}/T_{\rm peri})^{\gamma}}\,, \text{(regime II)} \quad (16)$$

where the functional form is motivated by the crossing time dependence on initial conditions shown in Fig 12, discussed below. A choice of $\gamma \approx 2.2$ ensures that at the boundary between regimes I and II, the fitted asymptote $T_{\rm asy} = 0.22\,T_{\rm peri}$ of regime I is matched. Using these constraints, the fitted decay rate τ' correlates with the

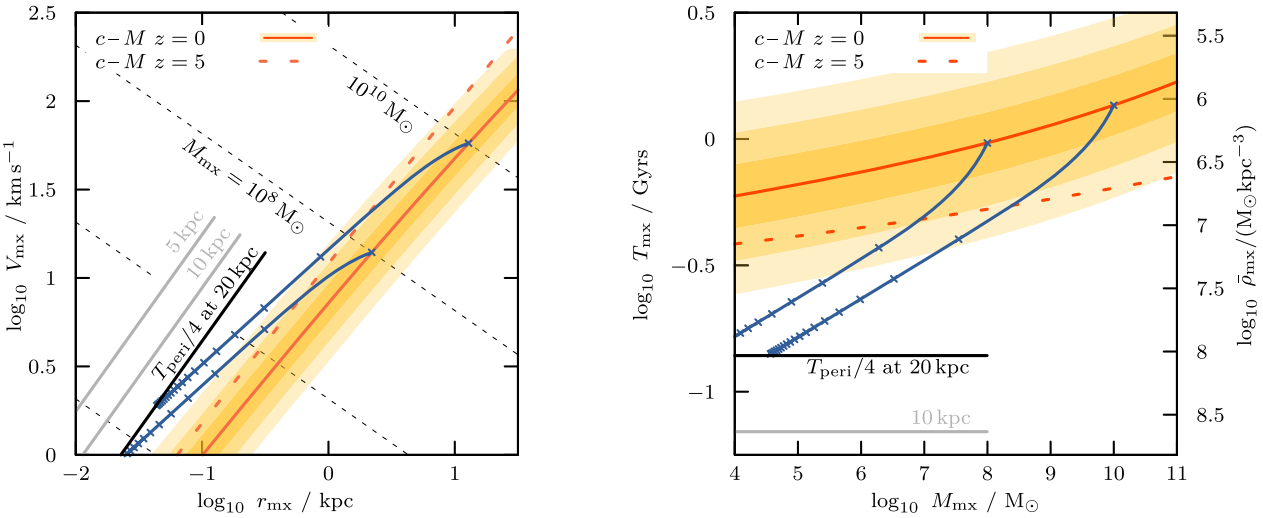

Figure 13. Tidal evolution in a cosmological context. The left-hand panel shows $\{r_{\rm mx}, V_{\rm mx}\}$ tidal evolutionary tracks (blue solid curves) for subhaloes of bound mass $M_{\rm mx} = 10^8\,\mathrm{M}_\odot$ and $10^{10}\,\mathrm{M}_\odot$ (i.e. virial masses and concentrations of $M_{200} = 3.8\times10^8\,\mathrm{M}_\odot$, $c = r_{200}/r_{\rm s}\approx 15$ and $3.5\times10^{10}\,\mathrm{M}_\odot$, $c\approx 11$, respectively.) with initial conditions consistent with the mean $z=0$ mass–concentration relation from Ludlow et al. (2014) (yellow shaded bands, for successive ±0.1 dex scatter in concentration). Ticks along the tracks correspond to intervals of one orbital period $T_{\rm orb}$ for a circular orbit with $r = 20$ kpc in an isothermal potential with circular velocity 220 km s^{-1} (or equivalently to 5 $T_{\rm orb}$ for 1:5 orbits, and 6.5 $T_{\rm orb}$ for 1:10 orbits with the same pericentre). For reference, the crossing times of asymptotic tidal remnants, $T_{\rm peri}/4$, is shown for values of $r_{\rm peri} = 5$ kpc, 10 kpc, 20 kpc. The panel on the right shows the same tidal tracks, but in terms of bound mass, $M_{\rm mx}$, and crossing time, $T_{\rm mx}$.

initial crossing time $T_{\rm mx0}/T_{\rm peri}$ roughly as

$$\tau'/T_{\rm orb} = 1.2(T_{\rm mx0}/T_{\rm peri})^{-1/2}\,. \qquad (17)$$

While these parameters were determined for circular orbits, the extension to eccentric orbits is straightforward through the delay factor $f_{\rm ecc}$ discussed in Section 3.3.

Fig. 12 compares $T_{\rm mx}$ measured from N-body snapshots after $n = 5$, 10, 15, and 20 orbital periods for different initial crossing times $T_{\rm mx0}/T_{\rm peri}$ against the empirical results of equation (15), showing good agreement between the model and the simulations. The functional dependence of the (near) asymptotic crossing time after $n = 20$ orbital periods on initial conditions is well described by a function of the form of equation (16), which imposes that for $T_{\rm mx0}/T_{\rm peri}\to 0$, $T_{\rm asy}\to T_{\rm mx0}$. In the regime where the subhalo is significantly denser than the host halo at pericentre, tidal evolution becomes negligible, as expected.

4 DISCUSSION

The results of the previous section may be used to provide some insight into ongoing discussions regarding substructure in CDM haloes and, in particular, on the abundance, structure, and spatial distribution of tidally stripped subhaloes. As discussed in Section 1, these discussions concern a wide variety of topics, from the ultimate survival of dark matter dominated systems, such as faint satellite galaxies, to the interpretation of distortions of strongly lensed galaxies, to theoretical expectations for a possible annihilation signal from surviving subhaloes. We plan to address some of these in future contributions, but provide here a first application to a few topical issues as illustration.

4.1 Tidal remnants in Milky Way-like systems

Our discussion so far has dealt with subhaloes with arbitrary values of $r_{\rm mx}$ and $V_{\rm mx}$, but these parameters are expected to be strongly correlated because of the redshift-dependent ΛCDM mass–concentration relation (see e.g. Ludlow et al. 2014, and references therein). This is shown, for illustration, in the left-hand panel of Fig. 13, where the solid red line indicates the mean relation at $z = 0$ and the shaded bands correspond to successive ±0.1 dex scatter in concentration. We also indicate, for completeness, the expected mean relation at $z = 5$ with a dashed red line.

ΛCDM subhaloes are constrained to move along the tidal track discussed in Section 3.4, two examples of which are shown by the blue curves in Fig. 13. One of them corresponds to a halo with initial $M_{\rm mx} = 10^{10}\,\mathrm{M}_\odot$ and the other to $M_{\rm mx} = 10^8\,\mathrm{M}_\odot$. Assuming that these haloes were placed on circular orbits in a potential like that of the Milky Way (represented crudely by equation 1) at $r = 20$ kpc, these subhaloes would be quickly stripped of mass (each tickmark on the tracks corresponds to one orbital period), and would gradually approach the asymptotic remnant stage, where $T_{\rm mx}\approx T_{\rm peri}/4$ (shown by the thick black line). We see from this that a $10^{10}\,\mathrm{M}_\odot$ halo would leave behind an asymptotic remnant with less than $10^5\,\mathrm{M}_\odot$, a characteristic radius of $r_{\rm mx}\sim 30$ pc and a maximum circular velocity of $V_{\rm mx}\sim 2$ km s^{-1}.

Such remnants are essentially impossible to properly resolve in direct cosmological simulations; indeed, a $10^{10}\,\mathrm{M}_\odot$ subhalo would be resolved with fewer than $\sim10^6$ particles in even some of the highest resolution simulations ever completed, such as those from the Aquarius project (Springel et al. 2008b). As discussed in the Appendix, a subhalo with 10^6 particles starts to deviate from the correct tidal track after being reduced to about than 1/100 of its initial mass, becoming increasingly prone to full (and artificial) tidal disruption. This implies that essentially no surviving $10^5\,\mathrm{M}_\odot$ haloes would be direct descendants of systems with initial mass of order $10^{10}\,\mathrm{M}_\odot$, as such systems would be most likely fully disrupted.

We note that this does not mean that the abundance of surviving $10^5\,\mathrm{M}_\odot$ haloes has been severely underestimated in simulations like Aquarius. Indeed, the abundance of low-mass subhaloes is vastly dominated by recently accreted low-mass subhaloes that have been

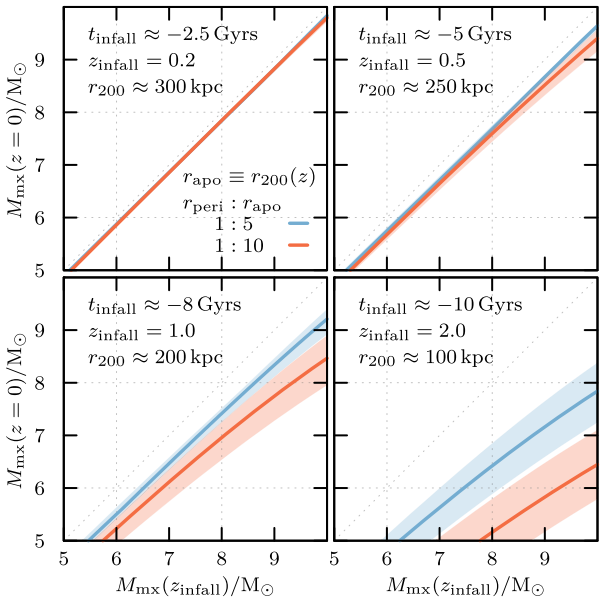

Figure 14. Initial versus final bound mass of ΛCDM subhaloes accreted at different times into an isothermal halo with circular velocity 220 km s^{-1}. Panels show the bound mass of subhaloes at $z = 0$ as a function of their mass at infall, for four different infall redshifts ($z = 0.2$, 0.5, 1.0, 2.0), and orbital eccentricities of 1:5 and 1:10. Subhaloes follow the mass–concentration relation at infall redshift, with shaded bands corresponding to ±0.1 dex scatter in concentration. The apocentre of the subhalo orbit $r_{\rm apo}$ is chosen to correspond to the virial radius r_{200} of the host halo at infall, as given in the legends. Note that subhaloes of bound mass $10^8 < M_{\rm mx}/{\rm M}_\odot < 10^{10}$, accreted 10 Gyr ago, have been stripped to less than 0.1 per cent of their initial mass on orbits with $r_{\rm peri} = 20$ kpc. Many such remnants would have been artificially disrupted in direct cosmological simulations.

only modestly stripped; in other words, there are simply too few 10^{10} M$_\odot$ systems to change the abundance of 10^5 M$_\odot$ subhaloes much (Springel et al. 2008b).

We also note that the comments above refer to the asymptotic tidal remnant of a subhalo, which is only reached after completing a fairly large number of orbits. In reality, most subhaloes have only had time to complete a few orbits, depending on their accretion time and their apocentric distance. We may use the time evolution model described in Section 3.6 to take this into account and to estimate the present-day mass of subhaloes accreted at different times during the evolution of a Milky Way-like halo. Since our main goal is to illustrate possible applications of our results, rather than to provide detailed predictions, we shall assume for this exercise that the host halo remains unchanged throughout and that it is well approximated by equation (1).

With this assumption, the virial radius of the host evolves 'passively' from $r_{200} \sim 100$ kpc at $z = 2$ to ∼300 kpc at present ('preudo-evolution', see Diemer, More & Kravtsov 2013). Assuming that the apocentric distance of subhaloes accreted at given redshift equals the host's current virial radius, Fig. 14 shows the predicted masses at $z = 0$ for subhaloes accreted at $z = 2$, 1, 0.5, and 0.2. Two curves are shown, for 1:5 (blue) and 1:10 (red) pericentre-to-apocentre ratios, respectively. 'Error bands' indicate the dispersion expected from the scatter in the mass–concentration relation (±0.1 dex in concentration).

In this illustration, most subhaloes accreted at $z \sim 0.2$ (the top left-hand panel of Fig. 14) have had time to complete at most one pericentric passage, and have therefore remained more or less unchanged since accretion. In contrast, subhaloes with infall mass $M_{\rm mx} = 10^{10}$ M$_\odot$ accreted at $z = 1$ have been stripped down to less than $\sim 10^9$ M$_\odot$, and those accreted at $z = 2$ to less than 10^8 M$_\odot$.

The evolution of massive ($M_{\rm mx} \gtrsim 10^8$ M$_\odot$) subhaloes that reach the inner regions of the Milky Way is of particular interest, as they could potentially host dwarf satellite galaxies that survive until the present. Fig 16 shows the evolution of subhalo mass $M_{\rm mx}$ as a function of time for subhaloes with initial masses of $M_{\rm mx0} = 10^8$ M$_\odot$ and $M_{\rm mx0} = 10^{10}$ M$_\odot$, for fixed pericentre distances of $r_{\rm peri} = 10$ kpc and 20 kpc. Most mass is lost within the first few Gyrs after accretion but even after 10 Gyr of evolution subhaloes as massive as 10^{10} M$_\odot$ should leave behind remnants with 10^7–10^8 M$_\odot$ at pericentric distances of order 20 kpc. These would be very poorly resolved – and maybe even missing – even in the best presently available cosmological hydrodynamical simulations, where the dark matter particle mass is typically of order $10^4 \sim 10^5$ M$_\odot$ (Oñorbe et al. 2015; Schaye et al. 2015; Sawala et al. 2016). This may have significant impact on ΛCDM predictions about the survival of faint satellites in the inner regions of the Milky Way, an issue that has attracted much interest in recent work, using cosmological simulations (e.g. Garrison-Kimmel et al. 2017; Richings et al. 2020), controlled simulations (e.g. Errani et al. 2017; Sanders et al. 2018; van den Bosch & Ogiya 2018; Errani & Peñarrubia 2020) and semi-analytical approaches (e.g. Stref et al. 2019).

4.2 Comparison with previous work

The tidal evolution of subhaloes in cosmological and controlled simulations has been studied extensively in previous work, and this section aims to compare the predictions of the rate of tidal stripping of the model of Section 3.6 to previous work.

4.2.1 Comparison with orbit-averaged mass-loss rates

The mass-loss rates of subhaloes in cosmological simulations have been studied by van den Bosch, Tormen & Giocoli (2005), who marginalize over all subhalo orbits, and propose a parametrization for the orbit-averaged mass-loss rate of the form (here reproduced using the notation of Jiang & van den Bosch 2016a):

$$ {\rm d}m/{\rm d}t = -\mathcal{A}\, m\, (m/M)^{\zeta}/\tau_{\rm dyn}\,, \qquad (18) $$

where m is a measure of the subhalo mass, M is a measure of the host halo mass, $\tau_{\rm dyn}$ is a measure for the crossing time of the host halo, and $\mathcal{A}$ and ζ are dimensionless constants.

For the parameters ζ and $\mathcal{A}$, Jiang & van den Bosch (2016a) measure values of $\zeta \sim 0.07$ and $\mathcal{A} \sim 1.3$, consistent with the earlier findings of Giocoli, Tormen & van den Bosch (2008). Hence, the average mass-loss as predicted by equation (18) is close to exponential, and $m \to 0$ for $t \to \infty$. Using the tidal tracks of Section 3.4, this also implies $T_{\rm mx} \to 0$ for $t \to \infty$.

While a direct comparison of the *orbit-averaged* mass-loss rates of equation (18) against the *orbit-specific* rates of the model of Section 3.6.2 is not straightforward, it is worth noting that the near exponential mass-loss described by equation (18) stands in stark contrast to the late-time behaviour described by the model of equation (12), which predicts surviving remnants of non-zero mass, characterized by a crossing time of $\sim T_{\rm peri}/4$, set by the crossing time of the host halo at pericentre. With the sole purpose of showing the qualitative behaviour, Fig. 16 shows as a black dotted curve the mass-loss rate as predicted from integrating equation (18), setting $\tau_{\rm dyn} = T_{\rm peri}$.

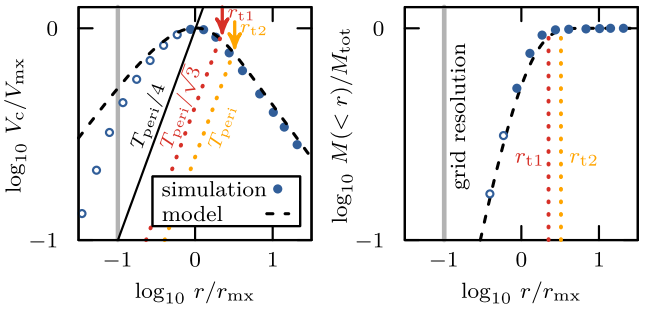

Figure 15. Circular velocity profile V_c (left-hand panel) and enclosed mass $M(< r)$ (right-hand panel) of a tidal remnant. Data from an N-body model ('simulation' – the top-right snapshot in Fig. 2) is shown using filled circles where unaffected by resolution, and using open circles where potentially affected by resolution. The analytical solution for a truncated NFW cusp (see equation 8) reproducing the measured $\{r_{mx}, V_{mx}\}$ is shown using black dashed curves ('model'). In the left-hand panel, the characteristic crossing time of $T_{peri}/4$ is shown using a solid black line, while the crossing times for two different simple definitions of tidal radii (r_{t1}, r_{t2}) are shown using red and orange dashed lines. The same tidal radii are also marked in the right-hand panel, showing that *beyond* the tidal radius lies only a small fraction of the total bound mass M_{tot}.

4.2.2 *Comparison with tidal radius approaches*

Various authors have modelled the rate of mass-loss to be proportional to the mass *outside* of some effective tidal radius r_t (Taylor & Babul 2001; Zentner & Bullock 2003; van den Bosch et al. 2005; Peñarrubia & Benson 2005; Diemand, Kuhlen & Madau 2007b, and more recently van den Bosch et al. 2018), i.e.

$$\mathrm{d}m/\mathrm{d}t = -\mathcal{B}\, m(> r_t)/T_{orb} \tag{19}$$

where $\mathcal{B}$ is a dimensionless constant. In this context, different recipes for the computation of the tidal radius have been proposed in the literature (e.g. Tormen, Diaferio & Syer 1998; Klypin et al. 1999; Peñarrubia & Benson 2005; Read et al. 2006) and are reviewed in van den Bosch et al. (2018). To first order, these tidal radii r_t are a measure for the region within the subhalo where the enclosed mean density is larger by some factor $\mathcal{C}$ than the enclosed mean density of the host halo at pericentre, e.g.

$$\bar{\rho}_{sub}(< r_t) = \mathcal{C}\, \bar{\rho}_{peri}\ . \tag{20}$$

In the following, we use $\mathcal{C} = 3$ and $\mathcal{C} = 1$ to define the two tidal radii r_{t1} and r_{t2}, shown in Fig. 15. Using this simple definition of tidal radius, as well as the mass-loss-dependent parametrization of the density profile discussed in Section 3.5, the mass evolution obtained from integrating equation (19) is plotted in Fig. 16 using blue-dashed curves. A value of $\mathcal{B} = 6$ approximately matches the initial mass evolution as computed from the model discussed in Section 3.6, and is consistent with the value measured by Diemand et al. (2007b). While the rate of mass-loss decelerates as the remnant bound mass decreases, mass-loss as described by the differential equation equation (19) in combination with the density profile evolution of equation (7) still eventually leads to fully disrupted tidal remnants, $m \to 0$ for $t \to \infty$.

The reason for this asymptotic behaviour is easily understood by noting that for mass-loss to stall ($\mathrm{d}m/\mathrm{d}t \to 0$), the differential equation equation (19) requires there to be no mass left outside the tidal radius, which is not met by the simple definitions of tidal radius of equation (20) in combination with the density profile parametrization of Section 3.5. The mass-loss model of equation (19) hence requires careful tailoring of the definition of tidal radius to the system in question, as discussed e.g. in van den Bosch et al. (2018). Specifically, to ensure a deceleration of tidal stripping that gives rise to a well-defined tidal remnant, a tidal radius definition is required which ensures that the mass beyond the tidal radius approaches zero sufficiently fast.

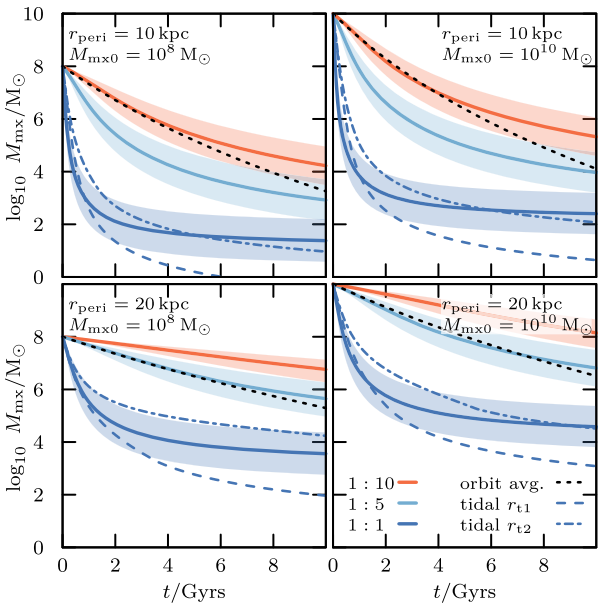

Figure 16. Evolution of bound mass on orbits of different eccentricity (equations 12 and 15). Panels show subhaloes with initial masses of 10^8 M$_\odot$ (left column) and 10^{10} M$_\odot$ (right column) on orbits with pericentric distances of 10 kpc (top row) and 20 kpc (bottom row). The shaded bands correspond to ± 0.1 dex scatter in the initial ($z = 0$) mass–concentration relation. Subhaloes on near-circular orbits with orbital radii of ~ 10 kpc are stripped by several decades in mass over 10 Gyrs. Black dotted curves ('orbit avg.') show the orbit-averaged mass-evolution fitted to cosmological simulations (equation 18, using parameters from Jiang & van den Bosch 2016a), and blue dashed curves ('tidal r_{t1}' and 'tidal r_{t2}') show the mass-evolution on circular orbits as computed from simple tidal radius arguments (equation 19), using the two tidal radii shown in Fig. 15.

4.3 Limitations of the model

Several aspects of the parametrization for tidal stripping discussed in this work adopt simplifications that should be considered carefully when applying the model to physical systems:

(i) The rate of mass-loss and the properties of the asymptotic remnant are set by the crossing time T_{peri} of the host halo at pericentre. This is only well defined if one assumes T_{peri} to be constant. This assumption is not valid for massive subhaloes, as dynamical friction would cause their orbits to decay, reducing their pericentric distances.

(ii) Our models describe the rapid tidal evolution towards a remnant with a well-defined characteristic crossing time. Tidal remnants in our models are resolved with a small number of particles, $N(< r_{mx}) \gtrsim 3000$, and have characteristic radii that are only a few times the grid size of our finest spatial grid, $r_{mx} \gtrsim 8\,\Delta x$. These numerical limitations complicate the interpretation of the long-term evolution of our models, and prevent us from distinguishing clearly between an asymptotic time-scale given by $T_{asy} = 0.22\, T_{peri}$ (suggested by fits of equation (10) to the combined results of all of our runs) and a slower 'secular' evolution beyond this time-scale. Assessing the long-term evolution of the tidal remnants using direct numerical simulations

requires better numerical resolution than the one adopted in our work.

(iii) Tidal stripping itself may cause changes to a subhalo's orbit because of asymmetries in the leading and trailing tidal stream and because of the self-gravity of the stream itself (see e.g. White 1983; Hernquist & Weinberg 1989, or more recently Fujii et al. 2006; Fellhauer & Lin 2007; Miller et al. 2020).

(iv) Our simulations are based on a static host halo, without response to the gravity of the subhalo. While this setup seems well motivated for systems where the host mass enclosed within $r_{\rm peri}$ is substantially larger than the mass of the subhalo, taking into account the host halo response will be important for mergers with larger host-to-subhalo mass ratios.

(v) The host halo model used in this study is a singular isothermal sphere, with a circular velocity chosen to approximate the Milky Way potential (equation 1). Tidal evolution in host haloes with substantially different radial dependence on the tidal field may affect the numerical values proposed for the crossing time of the asymptotic remnant $T_{\rm asy}$, the asymptotic decay rate $\tau_{\rm asy}$, and the eccentricity ' delay' factor $f_{\rm ecc}$.

(vi) All subhalo models considered were assumed to be collisionless, spherical, non-rotating, with an initially isotropic velocity dispersion.

(vii) Our results apply to the accretion of single subhaloes on to a smooth tidal field, and do not consider group infall: recent studies indicate that tidal stripping by *clumpy* tidal fields may increase the rates of tidal stripping (Stref et al. 2019; Delos 2019).

5 SUMMARY AND CONCLUSIONS

We have used *N*-body simulations of the tidal evolution of NFW haloes in the potential of a much more massive host to investigate the time evolution of tidal mass-loss, its dependence on orbital eccentricity and on the number of completed orbits, as well as the structural properties of the bound remnants. Our study also examines the effects of numerical limitations on the bound remnant structure, and the possibility that NFW subhaloes almost always leave behind a self-bound remnant.

Some of these issues have been addressed by earlier work, but our conclusions clarify and extend some of the earlier conclusions, and shed light on the long-term survival of NFW remnants in the regime of heavy tidal mass-loss. Our main conclusions may be summarized as follows.

The effect of tides on NFW subhaloes leads to a self-bound remnant whose asymptotic properties are set solely by initial subhalo structure and the properties of the host halo at the orbital pericentre. We identify two regimes, depending on the ratio between the initial characteristic crossing time (density) of the subhalo, $T_{\rm mx0}$, and the circular orbit time-scale (density) of the host at pericentre, $T_{\rm peri}$. Subhaloes with $T_{\rm mx0}/T_{\rm peri} < 2/3$ lose modest amounts of mass and approach asymptotically a remnant with a characteristic density set largely by its initial value.

On the other hand, subhaloes with $T_{\rm mx0}/T_{\rm peri} > 2/3$ lose large fractions of their initial mass and approach asymptotically a remnant whose characteristic time-scale is set solely by the host density at pericentre; i.e. $T_{\rm asy} \approx T_{\rm peri}/4$ (Fig. 10). This result suggests that NFW subhaloes are almost never fully disrupted, a result that may have important consequences on the long-term evolution and survival of luminous Milky Way satellites, as well as other implications for the studies of the distribution of dark matter on subgalactic scales.

As in earlier work, we find that the evolution of the characteristic parameters of the remnant (e.g. $r_{\rm mx}$ and $V_{\rm mx}$) depends solely on the total amount of mass lost, and that these parameters evolve along well-defined 'tidal tracks', independent of orbital eccentricity or of the number of orbits required to strip the system (Fig. 6). Our improved numerical resolution allows us to extend and revise the tidal tracks proposed in earlier studies.

Numerical limitations lead poorly resolved subhaloes to deviate systematically from this track, making them more susceptible to tidal mass-loss and possible full disruption. Such deviations may be used to identify remnants whose structure is not well converged numerically. Finite spatial resolution (e.g. grid size or 'softening'; Δx), as well as time resolution (e.g. minimum time-step) impose obvious limits on the size or characteristic time-scale of subhaloes that may be resolved. For example, systems where $r_{\rm mx}/\Delta x \lesssim 8$ deviate from convergence and are prone to artificial disruption, regardless of the number of particles used.

In otherwise well-resolved systems, the number of particles used to resolve the subhalo places the ultimate constraint: all subhaloes in our study start to deviate from convergence once they have been stripped to fewer than about 3000 particles inside $r_{\rm mx}$ (Fig. A1). This sets a high bar for the study of substructure in cosmological *N*-body simulations.

The shape of the mass profile of a tidally stripped subhalo deviates from the initial NFW shape, and is well described by an exponentially truncated NFW density profile (equation 7). The truncation 'radius' is set solely by the mass fraction that remains bound to the remnant. All heavily stripped NFW subhaloes thus converge asymptotically to the same mass profile shape, an exponentially truncated NFW cusp (Fig. 7).

The time evolution of the structural parameters of a subhalo may be well approximated by a simple function (equation 12) with a few scaling parameters that are well constrained by our simulation results. The main effect of orbital eccentricity is to 'delay' the evolution relative to subhaloes on circular orbits at equal pericentre. The delay factor, $f_{\rm ecc}$, is also well constrained by our simulation results (equation 4).

Our results thus provide a full description of the tidal evolution of NFW subhaloes, with the caveat that these results apply to the regime where the orbits have well-defined pericentric distances (i.e. the potential is approximately spherical and orbits are unaffected by tidal loss or dynamical friction) and the host potential does not evolve substantially with time. Although these caveats imply that our results cannot be used to make direct predictions for the properties of substructure in a ΛCDM halo, they can be used to interpret the results of cosmological simulations, and to identify their deficiencies and/or limitations. Our results may also be combined with cosmological simulations to place constraints on the abundance and structure of surviving subhaloes and on their relation with ultra-faint satellites and other dark matter-bound structures in the inner regions of the Galaxy. We plan to apply the lessons learned here to a number of pressing questions concerning substructure in CDM haloes in future contributions.

ACKNOWLEDGEMENTS

RE wants to thank J. Peñarrubia for discussions that were at the base of shaping ideas behind this work. We acknowledge useful discussions with Laura Sales, and thank the anonymous referee for detailed comments. RE also acknowledges support provided by a CITA National Fellowship and by funding from the European Research Council (ERC) under the European Union's Horizon 2020 research and innovation programme (grant no. 834148). This work used the DiRAC@Durham facility managed by the Institute for

Computational Cosmology on behalf of the STFC DiRAC HPC Facility (www.dirac.ac.uk). The equipment was funded by BEIS capital funding via STFC capital grant nos ST/K00042X/1, ST/P002293/1, ST/R002371/1 and ST/S002502/1, Durham University and STFC operations grant no. ST/R000832/1.

DATA AVAILABILITY

The data underlying this article will be shared on reasonable request to the corresponding author.

REFERENCES

Boylan-Kolchin M., Springel V., White S. D. M., Jenkins A., 2010, MNRAS, 406, 896
D'Onghia E., Springel V., Hernquist L., Keres D., 2010, ApJ, 709, 1138
Delos M. S., 2019, Phys. Rev. D, 100, 083529
Despali G., Vegetti S., 2017, MNRAS, 469, 1997
Diemand J., Kuhlen M., Madau P., 2007a, ApJ, 657, 262
Diemand J., Kuhlen M., Madau P., 2007b, ApJ, 667, 859
Diemer B., More S., Kravtsov A. V., 2013, ApJ, 766, 25
Eilers A.-C., Hogg D. W., Rix H.-W., Ness M. K., 2019, ApJ, 871, 120
Erkal D., Belokurov V., 2015, MNRAS, 450, 1136
Errani R., Peñarrubia J., 2020, MNRAS, 491, 4591
Errani R., Peñarrubia J., Laporte C. F. P., Gómez F. A., 2017, MNRAS, 465, L59
Fellhauer M., Lin D. N. C., 2007, MNRAS, 375, 604
Fellhauer M., Kroupa P., Baumgardt H., Bien R., Boily C. M., Spurzem R., Wassmer N., 2000, New Astron., 5, 305
Frenk C. S., White S. D. M., 2012, Annalen der Physik, 524, 507
Fritz T. K., Battaglia G., Pawlowski M. S., Kallivayalil N., van der Marel R., Sohn S. T., Brook C., Besla G., 2018, A&A, 619, A103
Fujii M., Funato Y., Makino J., 2006, PASJ, 58, 743
Gaia Collaboration et al., 2018, A&A, 616, A12
Garrison-Kimmel S. et al., 2017, MNRAS, 471, 1709
Ghigna S., Moore B., Governato F., Lake G., Quinn T., Stadel J., 1998, MNRAS, 300, 146
Giocoli C., Tormen G., van den Bosch F. C., 2008, MNRAS, 386, 2135
Green A. M., 2005, New Astron. Rev., 49, 181
Green S. B., van den Bosch F. C., 2019, MNRAS, 490, 2091
Hayashi E., Navarro J. F., Taylor J. E., Stadel J., Quinn T., 2003, ApJ, 584, 541
Hernquist L., Weinberg M. D., 1989, MNRAS, 238, 407
Ibata R. A., Lewis G. F., Irwin M. J., Quinn T., 2002, MNRAS, 332, 915
Jiang F., van den Bosch F. C., 2016a, MNRAS, 458, 2848
Jiang F., van den Bosch F. C., 2016b, MNRAS, 458, 2848
Johnston K. V., Spergel D. N., Haydn C., 2002, ApJ, 570, 656
Klypin A., Gottlöber S., Kravtsov A. V., Khokhlov A. M., 1999, ApJ, 516, 530
Kravtsov A. V., Gnedin O. Y., Klypin A. A., 2004, ApJ, 609, 482
Lavalle J., Pochon J., Salati P., Taillet R., 2007, A&A, 462, 827
Li T. S. et al., 2018, ApJ, 866, 22
Ludlow A. D., Navarro J. F., Springel V., Jenkins A., Frenk C. S., Helmi A., 2009, ApJ, 692, 931
Ludlow A. D., Navarro J. F., Angulo R. E., Boylan-Kolchin M., Springel V., Frenk C., White S. D. M., 2014, MNRAS, 441, 378
Miller T. B., van den Bosch F. C., Green S. B., Ogiya G., 2020, MNRAS, 495, 4496
Moore B., Ghigna S., Governato F., Lake G., Quinn T., Stadel J., Tozzi P., 1999, ApJ, 524, L19
Navarro J. F., Frenk C. S., White S. D. M., 1996, ApJ, 462, 563
Navarro J. F., Frenk C. S., White S. D. M., 1997, ApJ, 490, 493
Ogiya G., van den Bosch F. C., Hahn O., Green S. B., Miller T. B., Burkert A., 2019, MNRAS, 485, 189
Oñorbe J., Boylan-Kolchin M., Bullock J. S., Hopkins P. F., Kereš D., Faucher-Giguère C.-A., Quataert E., Murray N., 2015, MNRAS, 454, 2092
Peñarrubia J., Benson A. J., 2005, MNRAS, 364, 977
Peñarrubia J., Navarro J. F., McConnachie A. W., 2008, ApJ, 673, 226
Peñarrubia J., Benson A. J., Walker M. G., Gilmore G., McConnachie A. W., Mayer L., 2010, MNRAS, 406, 1290
Planck Collaboration et al., 2020, A&A, 641, A6
Power C., Navarro J. F., Jenkins A., Frenk C. S., White S. D. M., Springel V., Stadel J., Quinn T., 2003, MNRAS, 338, 14
Read J. I., Wilkinson M. I., Evans N. W., Gilmore G., Kleyna J. T., 2006, MNRAS, 366, 429
Richings J. et al., 2020, MNRAS, 492, 5780
Sanders J. L., Evans N. W., Dehnen W., 2018, MNRAS, 478, 3879
Sawala T. et al., 2016, MNRAS, 457, 1931
Schaye J. et al., 2015, MNRAS, 446, 521
Simon J. D., 2018, ApJ, 863, 89
Springel V. et al., 2008a, MNRAS, 391, 1685
Springel V. et al., 2008b, Nature, 456, 73
Stref M., Lacroix T., Lavalle J., 2019, Galaxies, 7, 65
Tasitsiomi A., Olinto A. V., 2002, Phys. Rev. D, 66, 083006
Taylor J. E., Babul A., 2001, ApJ, 559, 716
Tormen G., Bouchet F. R., White S. D. M., 1997, MNRAS, 286, 865
Tormen G., Diaferio A., Syer D., 1998, MNRAS, 299, 728
van den Bosch F. C., Ogiya G., 2018, MNRAS, 475, 4066
van den Bosch F. C., Tormen G., Giocoli C., 2005, MNRAS, 359, 1029
van den Bosch F. C., Ogiya G., Hahn O., Burkert A., 2018, MNRAS, 474, 3043
Vegetti S., Koopmans L. V. E., 2009, MNRAS, 400, 1583
Wang J., Frenk C. S., Navarro J. F., Gao L., Sawala T., 2012, MNRAS, 424, 2715
Wang J., Bose S., Frenk C. S., Gao L., Jenkins A., Springel V., White S. D. M., 2020, Nature, 585, 39
Weinberg M. D., 1994, AJ, 108, 1398
White S. D. M., 1983, ApJ, 274, 53
White S. D. M., Rees M. J., 1978, MNRAS, 183, 341
Zentner A. R., Bullock J. S., 2003, ApJ, 598, 49

APPENDIX: NUMERICAL CONVERGENCE

Numerical resolution imposes strong limits on the ability of simulations to follow the tidal evolution of subhaloes. Most critical are the finite time-stepping, spatial resolution, and number of particles used in a simulation. We explore in this Appendix the impact of such limitations and the constraints they place on our results.

As stated in Section 2.4, our simulations evolve subhaloes with a single, constant time-step set to $\Delta t = 0.025 \times \min(T_{\rm mx0}, T_{\rm peri})$. This time-step is shown as a dashed diagonal line in Fig. 3 ($\times 10$ to fit in the figure) and is clearly much shorter than the subhalo crossing time at a radius equal to the best grid spatial resolution, $\sim r_{\rm mx0}/128$. Fixing the time-step this way reduces the dimensionality of the problem, leaving only the spatial (grid) resolution and the number of particles for us to consider.

To do so, we perform two series of simulations: one where we fix the number of subhalo particles to $N = 10^7$, the maximum in our runs, and vary the grid size systematically from $\Delta x \approx r_{\rm mx0}/128$ to $r_{\rm mx0}/32$; and another where we fix Δx to $r_{\rm mx0}/128$ and vary the number of particles from 10^7 to 10^5. We choose for these tests subhaloes on 1: 5 eccentric orbits ($r_{\rm peri} = 40\,{\rm kpc}$) with initial crossing times $0.5 < T_{\rm mx0}/T_{\rm peri} < 2$.

The 'tidal tracks' that result are shown in Fig. A1. Each symbol corresponds to parameters measured at a successive apocentric passage, normalized to the initial values. The left-hand panel shows the effect of varying the grid size. As the spatial resolution deteriorates, subhaloes deviate systematically from the converged tidal track (indicated by the dashed black curve) towards longer crossing times and lower characteristic densities. The arrows indicate the radius corresponding to $r_{\rm mx} = 8\Delta x$, which, in each case, is a good diagnostic

of the minimum 'size' a subhalo must have for its characteristic parameters to be properly resolved. More precisely, subhaloes with $r_{\rm mx} < 8\Delta x$ have characteristic time-scales, $T_{\rm mx}$, that deviate more than 10 per cent from the time-scale expected from the tidal track.

The right-hand panel of Fig. A1 is analogous to the one on the left, but for the series of runs where the number of particles is varied. The arrows in this case indicate the location of subhaloes where the number of particles inside $r_{\rm mx}$, $N_{\rm mx} = M_{\rm mx}/m_{\rm p}$, drops below ∼3000 (here m_p is the mass per particle). This simple criterion again identifies the minimum number of particles needed to resolve the characteristic parameters of a tidally affected NFW subhalo, in the sense than tidal remnants with $N_{\rm mx} < 3000$ typically have crossing times that deviate by more than 10 per cent from the converged tidal track. The analysis throughout the paper is based on results obtained for subhaloes that satisfy simultaneously both criteria (i.e. $r_{\rm mx} > 8\Delta x$ and $N_{\rm mx} > 3000$).

For our simulations with $N = 10^7$ and $\Delta x \approx r_{\rm mx0}/128$, resolution is mainly limited by the grid size, and the condition $r_{\rm mx} > 8\Delta x$ implies that numerical limitations begin to dominate once $M_{\rm mx}$ has been reduced to about 0.3 per cent of its initial value. This sets the limits of the most highly stripped system effectively probed by our simulations: $M_{\rm mx}/M_{\rm mx0} \approx 1/300$; or $V_{\rm mx}/V_{\rm mx0} \approx 1/5$; or $r_{\rm mx}/r_{\rm mx0} \approx 1/16$; or $T_{\rm mx}/T_{\rm mx0} \approx 1/3$.

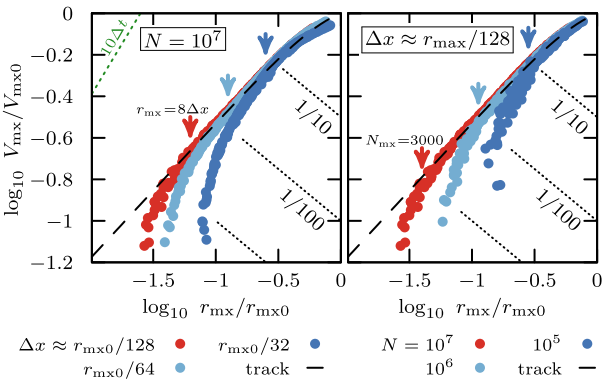

Figure A1. *Left:* Evolution of $r_{\rm mx}$ and $V_{\rm mx}$ for 10^7-particle haloes run with three different grid sizes for the highest resolution mesh. Note that systems start to deviate from the tidal track (shown with a dashed black curve, equation 5) when the characteristic radius of the remnant approaches $r_{\rm mx} \approx 8\,\Delta x$. *Right:* same as left, but for a series of runs with fixed time and spatial resolution, but varying the number of particles of the initial halo. Note that remnants artificially deviate systematically from the tidal track when the remnant is resolved with fewer than ∼3000 particles within $r_{\rm mx}$.

This paper has been typeset from a TEX/LATEX file prepared by the author.